UNIVERSIDADE DA BEIRA INTERIOR
Engenharia

Numerical simulation of the MYRRHA reactor design v1.6

Sandra Maria Mendes Gonçalves

Dissertação para a obtenção do Grau de Mestre em
Engenharia Aeronáutica
(Ciclo de estudos integrado)

Orientador: Prof. Doutor Francisco Miguel Ribeiro Proença Brójo
Co-orientadora: Doutora Lilla Koloszar

Covilhã, setembro de 2017

Dedication

Dedicated to my mother, Yolanda Gonçalves, who devoted her life to me. Without her it would have been impossible to complete this achievement.

"What if I fall? Oh, but my darling, what if you fly?"

Erin Hanson

Acknowledgements

Resumo

Este estudo está inserido no âmbito do projecto do reactor MYRRHA, desenvolvido pelo Centro de Investigação Nuclear Belga (SCK-CEN), ao qual o VKI está a dar a sua contribuição. Esta dissertação tem como objectivo realizar uma simulação numérica da versão 1.6 do reactor MYRRHA e analisar os seus resultados. É importante notar que parte das fontes de informação são confidenciais.

O metal líquido pesado considerado é o LBE (Lead Bismuth Eutectic). Este reactor tem originalmente uma geometria complexa, que foi simplificada para fins de simulações.

O estudo é feito através de um modelo monofásico de Dinâmica de Fluidos Computacional em condições nominais do circuito do líquido de refrigeração primário. Tem como objectivo fornecer uma descrição do fluxo e dos campos de temperatura do ciclo inteiro, enquanto os padrões do fluxo desenvolvidos na parte superior e inferior do MYRRHA v1.6 são analisados da forma mais completa possível, usando um modelo de regime permanente. O modelo foi preparado com recurso ao software OpenFOAM, dada a sua natureza de software aberto. Primeiro, as condições numéricas são estipuladas, depois os meios porosos são definidos, e finalmente é feita a modelação térmica.

O *solver* usado nestas simulaçõees para realizar a modelação térmica é o *myrrhaSimpleFoam*, desenvolvido no von Karman Institute e complementado com os mais importantes modelos turbulentos térmicos para líquidos com baixo número de Prandtl actualmente. O modelo de turbulência aplicado é o *Standard* $\kappa - \varepsilon$ e, de forma a prever os efeitos turbulentos de transferência de calor, a analogia Reynolds é implementada, considerando um número de Prandtl constante de 2.0. O fluxo é caracterizado por ser constante, incompressível e turbulento. Dada a natureza turbulenta do fluido, as equações são baseadas no modelo RANS.

Finalmente, é feita uma comparação com os resultados de um estudo anterior, referente ao design v1.4 do reactor.

Palavras-chave

Reactor nuclear, Simulações Numéricas, CFD, OpenFOAM, Metal Líquido Pesado

Abstract

This study is embodied in the project of MYRRHA reactor, developed by the Belgian Nuclear Research Center (SCK-CEN), to which VKI is giving its contribution. This dissertation aims to perform a numerical simulation of the MYRRHA reactor design version 1.6 and analyse its results. It is important to point out that part of the information sources are confidential.

The heavy metal considered is LBE (Lead Bismuth Eutectic). This reactor has originally a complex geometry, which was simplified for simulation purposes.

The investigation is made through a single-phase flow CFD model in nominal conditions of the primary coolant circuit. Its objective is to provide a description of the flow and temperature fields of the entire pool loop while analysing the flow patterns that develop in the lower and the upper plenum of the MYRRHA v1.6 facility as complete as possible, while using a steady-state model. The model was prepared in the OpenFOAM software, due to its open source nature. Firstly the numerical set up is made, then the porous media is defined and finally the thermal modelling takes place.

The solver used in these simulations to perform the thermal modelling is *myrrhaSimpleFoam*, developed at von Karman Institute and complemented with the most relevant thermal turbulence models for low Prandtl number liquids currently. The turbulence model applied is the *Standard* $\kappa - \varepsilon$ and, in order to predict the effects of turbulent heat transfer, the Reynolds analogy is implemented, with a constant turbulent Prandtl number of 2.0. The flow is characterized for being steady state, incompressible and turbulent. Since we are dealing with a turbulent flow, the equations are solved based on the Reynolds Averaged Navier-Stokes (RANS) model.

Finally, a comparison with the results from a previous study involving the design v1.4 of the reactor is made.

Keywords

x

Contents

List of Figures

List of Tables

List of Acronyms

ACS	Above Core Structure
ADS	Accelerator driven systems
CFD	Computational Fluid Dynamics
CHT	Conjugated Heat Transfer
CPU	Central Processing Unit
CR	Control rods
CRS	Core Restraint System
CHT	Conjugated heat transfer
CSP	Core Support Plate
CSS	Core Support Structure
DNS	Direct Numerical Simulation
EU	European Union
FA	Fuel Assembly
FDM	Finite difference method
FEM	Finite element method
FVM	Finite volume method
HLLW	High level long-lived radioactive waste
HP	Hot Plenum
HX	Heat exchanger
IPS	In-Pile-Sections
IVFHM	In-Vessel Fuel Handling Machine
LBE	Lead-Bismuth Eutectic
LES	Large Eddy Simulation
LLFPs	Long-lived fission products
MAs	Minor actinides
MPSOCD	Multi-objective Particle Swarm Optimization Crowding Distance
MYRRHA	Multi-purpose hybrid research reactor for high-tech application
OpenFOAM	Open Source Field Operation and Manipulation
PIMPLE	Merged SIMPLE and PISO
PISO	Pressure-implicit split-operator
PHX	Primay heat exchanger
P&T	Partitioning and Transtumation
RANS	Reynolds-Averaged Navier-Stokes
R&D	Research and Development
SCK-CEN	Studiecentrum voor Kernenergie – Centre d'étude de l'énergie nucléaire
SIMPLE	Semi-implicit method for pressure-linked equations
SNE-TP	Sustainable Nuclear Energy Technology Platform
SRA	Strategic research agenda
SR	Safety rods
UBI	Universidade da Beira Interior
VKI	von Karman Institute

Nomenclature

$A_{exchange}$	Water tubes' exchange surface	$[m^2]$
A	Area	$[m^2]$
$C_{2,r}$	Inertial radial resistance coefficient	$[m^{-1}]$
$C_{2,y}$	Inertial axial resistance coefficient	$[m^{-1}]$
C_p	Specific heat	$[Jkg^{-1}.K^{-1}]$
D_u	Hydraulic diameter	$[m]$
D_r	Clad outside diameter	$[m]$
D_w	Wire diameter	$[m]$
d	Darcy coefficient	$[m^{-2}]$
E	Wall roughness parameter	$[-]$
F_{HX}	Factor to adjust the heat that is removed in the PHX	$[-]$
F	Geometrical factor	$[-]$
G	Gravity term	$[m/s^2]$
h_e	Heat transfer coefficient (LBE side)	$[W/m^2.K]$
h_i	Heat transfer coefficient (Water side)	$[W/m^2.K]$
I_U	Turbulence Intensity	$[\%]$
$\dot{m}$	Mass flow rate	$[Kg/s]$
$\Bbbk$	von Karman constant	$[-]$
N_r	Number of pins	$[-]$
Nu	Nusselt number	$[-]$
l	Turbulence length scale	$[-]$
L	Reference length	$[m]$
L_pin	Pin length	$[m]$
P/D	Pitch to diameter ratio	$[-]$
p	Pressure	$[bar]$
Pe	Peclet number	$[-]$
Pr	Prandtl number	$[-]$
Pr_t	Turbulent Prandtl number	$[-]$
$\dot{q}$	Heat flux	$[W/m^2]$
Q_core	Core heat source distribution	$[W/m^3]$
Q	Volumetric flow	$[m^3/s]$
R	Heat transfer resistance	$[K/W]$
Re	Reynolds number	$[-]$
S	Heat sink	$[-]$
S_{PHX}	Volumetric heat sink	$[-]$
S_t	Stanton number	$[-]$
t	Time	$[s]$
$T - T_{water}$	Local temperature difference between the LBE and the water	$[K]$
T	Temperature	$[K]$
u, v, w	Velocity components according to x, y and z	$[m/s]$
U	Velocity	$[m/s]$
$\mathcal{V}$	Viscous term	$[-]$
V	Volume	$[m^3]$

Greek letters

α	Thermal diffusivity	$[m^2/s]$
α_t	Turbulent thermal diffusivity	$[m^2/s]$
μ	Dynamic viscosity	$[Pa \cdot s]$
μ_t	Turbulent dynamic viscosity	$[Pa \cdot s]$
μ_τ	Local wall shear stress	$[Pa]$
ν	Kinematic turbulent viscosity	$[m^2/s]$
π	Constant of value 3.14159...	$[-]$
ρ	Density	$[kg/m^3]$
ε	Rate of dissipation of turbulent kinetic energy	$[m^3.s^{-3}]$
λ	Thermal conductivity	$[W/m.K]$
κ	Turbulent kinetic energy	$[m^2.s^{-2}]$
κ_i	Turbulent kinetic energy at inlet	$[m^2.s^{-2}]$
β	Forchheimer coefficient	(m^{-1})
ω	Permeability coefficient	(m^2)
γ	Porosity coefficient	$(-)$
Γ_t	Turbulent or eddy diffusivity	$(m^2.s^{-1})$
σ_t	Turbulent Prandtl/Schmidt	$(-)$

It should be noted that some symbols have duplicate meaning. However, each symbol meaning is referenced according to its context throughout the text.

Chapter 1

Introduction

The MYRRHA project emerged from the necessity to replace BR2 MTR reactor, a flexible irradiation facility, in operation since 1962. MYRRHA is intended to be innovative and supportive of future oriented research projects.

This Multi-purpose hybrid research reactor for high-tech applications aims to be a flexible fast spectrum nuclear reactor.

1.1 Motivation

This project arose the author's interest mainly due to its current character, its numerical nature and relation with environmental issues. The fact that an opportunity to learn how to work with OpenFOAM emerged also contributed to the author's enthusiasm, along with the chance to be enrolled in an internship at VKI.

The management of high-level long-lived radioactive waste (HLLW), originated by the reprocessing of used nuclear fuels, is one of the biggest problems at international level regarding nuclear energy. Currently, the solution is geological disposal of the waste, which includes minor actinides (MA) like Np, Am, Cm and long-lived fission products (LLFPs).

Geological disposal consists in isolating the wastes in engineered barriers in deep stable rocks, with the objective of decaying all the radioactive material within the repository or in the surrounding rocks. However, it is scientifically impossible to assure that no concentrations, even though in small amounts, will migrate into the environment in far future, threatening the safety of the living beings [1]. Consequently, this originates problems of public acceptance, creating the need to find an alternative solution.

Mukaiyama (1994) presented an appealing strategy named partitioning and transmutation (P&T). This concept aims to separate long-lived nuclides from the waste stream and to shorten their lives or even convert them into non-radioactive nuclides [2]. Accelerator driven transmutations systems (ADS) can be effective with the P&T strategy due to its flexibility of designing. Worldwide research and development (R&D) of the P&T strategy has been made, in the frame of the Generation IV (GEN IV), aiming to reduce the impact of geological disposal.

One of the MYRRHA project goals is to diminish the amount, half-life and toxicity of the nuclear waste. The SNE-TP community, along with the EU vision document and the strategic research agenda o the SNE-TP, have pointed out some demands, such as:

- The need to develop an alternative coolant technology being lead or gas.

- In both EU vision document and in the SRA of the SNE-TP, the importance of a demonstration of the ADS concept in Europe was indicated. In order to clarify the potential of the accelerator-driven (hybrid) reactor systems to burn the MAs and the LLFPs, studies have been held in both France and Japan [3].

- The importance of a front-runner position of Europe for Gen IV reactor development, stated in the vision document and in the SRA.

In conclusion, the technological development of the fuel and materials of these concepts request the availability of a flexible fast spectrum irradiation facility.

Taking into account all of these European and International demands, considering demonstration and irradiation capabilities, MYRRHA is proposed by SCK-CEN as a flexible fast spectrum irradiation facility able to operate in subcritical and critical mode, piloted by a particle accelerator ADS (Accelerator Driven System). This makes this project a global pioneer demonstration project for a new type of reactor. VKI's role is to act as a CFD support to the SCK-CEN front line engineering.

1.2   Objectives

This work aims to perform a numerical simulation of the MYRHHA version 1.6, while recurring to the OpenFOAM software.

The first step is to generate and obtain a proper mesh of the geometry with the desired defined regions. The second step is to do the numerical set up, according to nominal conditions and while implementing the *myrrhaSimpleFoam* solver to obtain the thermal-hydraulic description of the reactor. Finally, a comparison is with the results of a previous study [4] involving design v1.4 of MYRRHA. The aim of this comparison is to verify the differences between both models.

The simulation was considered as a steady-state problem as it requires less CPU time to be completed.

Chapter 2

Computational Fluid Dynamics

The present chapter contains an overview of the Computational Fluid Dynamics (CFD) concept. CFD is "the analysis of systems involving fluid flow, heat transfer and associated phenomena such as chemical reactions by means of computer-based simulation" [5]. Recently, along with technology exponential growth, CFD modelling has also increased.

2.1 About CFD

There are three aproaches to solve a problem in fluid mechanics and heat transfer: experimental, theoretical and computational. The latter one is the method used in the present work.

The cost of CFD is usually more affordable than the cost of a high-quality experimental facility. Concerning fluid systems design, CFD offers multiple unique advantages over experiment-based approaches:

- Substantial reduction of lead-times and costs of new designs

- Ability to study systems where controlled experiments are difficult or impossible to perform (for instance, very large systems)

- Ability to study systems under hazardous conditions at and beyond their normal performance limits (for instance, safety studies and accident scenarios)

- Practically unlimited level of detail of results

CFD codes are based on algorithms capable of facing fluid flow problems. All codes consist of three main elements, which are overview in the following subsections 2.1.1, 2.1.2 and 2.1.3. These are:

1. Pre-processor

2. Solver

3. Post-processor

Despite all the advantages mentioned before, experimentation continues to be crucial, especially when the flows in study are very complex. In fact, in most fluid flow and heat transfer design situations, experimental testing is necessary [6]. Along with computer studies, the range of conditions over which testing is demanded can be reduced.
CFD also presents disadvantages like:

- Computer storage and costs;

- Speed;

- The difficulty to understand and mathematically model some complex phenomena;

- The inability to solve certain flow problems involving complex physical processes;

- Truncation erros;

- Boundary condition problems

However, with the advance of computer hardware and algorithms, these might be overcome in the future.

2.1.1   Pre-processor

The pre-processor consists of the input of a flow problem to a CFD program while using an operator-friendly interface and subsequent transformation to be used by the solver. In the present work, as stated before, the program used is OpenFOAM. In this step the user:

- Defines the geometry of the region of interest (computational domain), being the reactor the geometry defined in the present study;

- Generates the grid, which consists of the sub-division of the domain into a number of smaller, non-overlapping sub-domains, creating a mesh of cells (or control volumes). In OpenFOAM this grid is referred to as *polyMesh*;

- Finally, selects the physical and chemical phenomena that need to be modelled, defines the fluid properties and specifies the appropriate boundary conditions at cells, which coincide with or touch the domain boundary.

The nodes inside each cell contain the defined solution to a flow problem (velocity, pressure, etc.). The number of cells in the mesh defines the accuracy of a CFD solution, thus normally, the larger the number, the more accurate is the solution. Another contributing factor to the accuracy of the solution is the fineness of the grid. In the areas where large variations occur from point to point the mesh should be finer, while in the regions with minor changes it should be coarser. Therefore, ideal meshes are non-uniform. The obtainment of a good mesh highly depends on the skills of the CFD user to design a mesh that complies with the desired accuracy and solution cost.

2.1.2   Solver

There are three different streams of numerical solution techniques: finite difference method (FDM), finite element method and (FEM) spectral methods. In the case of CFD, the method used is the finite volume method (FVM), a particular finite difference formulation, which is described in 2.2.1 . The numerical algorithm involves the following steps:

1. Integration of the governing equations of fluid flow over all the (finite) control volumes of the domain;

2. Discretisation – conversion of the resulting integral equations into a system of algebraic equations;

3. Solution of the algebraic equations by an iterative method.

The process to reach a solution is iterative due to the complexity and non-linearity of the physical phenomena.

4

Examples of solution procedures are: SIMPLE algorithm (ensures correct linkage between pressure and velocity), Gauss-Seidel (multigrid accelerators and conjugate gradient methods), TDMA (tri-diagonal matrix algorithm) [5]. In the case in study, the solver used is myrrhaSimpleFoam.

2.1.3 Post-processor

Nowadays, foremost CFD softwares have data visualisation tools. In the OpenFOAM case, this tool is called *paraview*. These tools include:

- Domain geometry and grid display

- Vector plots

- Line and shaded contour plots

- 2D and 3D surface plots

- Particle tracking

- View manipulation (translation, rotation, scaling etc.)

- Colour PostScript output

Once the solution of the fluid flow problem is obtained, the complexity of the physics needs to be taken into account and the results should comply with it. Before the set up and running of the CFD simulation, the physical and chemical phenomena identification and formulation of the flow need to be considered.

Assumptions need to be made to reduce the complexity to a controllable level of the case whilst maintaining the salient features of the problem in study. Therefore, good modelling skills are desirable in order to obtain a good quality of the CFD post-processing, as the suitability of the simplifications introduced at this stage is partly responsible for that quality. Consequently, the user should be mindful of all the assumptions that have been made.

The specifications of the domain geometry and grid design are the main tasks at the input stage and a good result is characterised by convergence and grid independence. As stated before, the process is iterative, and in a converged solution the residuals are very small. A converged solution can be achieved by carefully selecting the settings of various relaxation factors and acceleration devices.

There are no exact processes and guidelines to make these selections since they depend on the study case. However, experience with the code in use is a very contributing factor to optimise the solution, which can be obtained with extensive use. Likewise, it is not possible to predict the errors introduced by inadequate grid design for a general flow. To obtain a good initial grid design, the expected properties of the flow should be analysed. Once again, experience is a valuable factor in gridding. Background in the fluid dynamics of the problem is also helpful. In what comes to eliminating errors due to coarseness of a grid, the only way is to conduct a grid dependence study, consisting in successive refinement of an initially coarse grid until a certain point where key results do not change. Once this point is reached, the simulation becomes grid independent, which is something essential in all high-quality CFD studies. Finally, it is possible to conclude that experience and a full understanding of the physics of fluid flows and the fundamentals of the numerical algorithms are essential to succeed in CFD[5].

The fluid is considered to be continuum and its behaviour is described according to its macroscopic properties (velocity, pressure, density and temperature, and space and time derivatives), ignoring the molecular structure and molecular motions. Therefore, a particle or point in a fluid is the smallest possible element of fluid whose macroscopic properties are independent from individual molecules, being averages over suitably large number of molecules.

2.2 OpenFOAM

The software used to develop the numerical simulations related to the present work is OpenFOAM, Open Source Field Operation and Manipulation, version 3.0.1, an open source software for computational fluid dynamics owned by the OpenFOAM Foundation [7]. Its modular structure of C++ libraries allows users to create and modify executable files (applications) divided in solvers and utilities. Solvers are designed to a specific problem in continuum mechanics. Utilities are designed to deal with data manipulation. The user is free to create new solvers and utilities, although some knowledge regarding methods, physics and programming techniques is required. This software ofers pre and post-processing environments, being their interfaces OpenFOAM utilities.

2.2.1 Finite Volumes Method

OpenFOAM is based on the finite volume method [8]. As referrenced in 2.1.2, the first step of control volume integration, differentiates the finite volume method from the rest of CFD tecnhiques [5]. It solves the partial differential equations representing conservation laws over differential volumes into discrete algebraic equations over finite volumes (or elements or cells). Similarly to the finite difference or finite element method, firstly the discretization of the geometric domain is made to reach the solution. In the FVM case, the domain is discretized into non-overlapping elements or finite volumes. The sysyem of partial differential equations is discretized into algebraic equations by integrating them over each discrete element. Then, the system is solved to compute the values of the dependent variable for each of the elements.

The FVM is a conservatie method, as the flux entering a certain volume is the same as the one leaving the adjacent volume. Besides, it can also be formulated in the pysical space on any structured or unstructured mesh. Therefore, there are no obstacles regarding the transformation between the physical and the computational coordinate system. [9]. These properties make the FVM suitable for the simulation of flows involving complex geometries. Moreover, in the FVM, the implementation of boundary conditions is simple and noninvasive as the unknown variables are evaluated at the centroid of the volume elements and not at their boundary faces [8]. The conservation of a general flow variable φ (for example a velocity component or enthalpy) inside a finite control volume can be expressed as a balance between the numerous processes tending to increase or decrease it.

However, the FVM presents one disadvantage compared to the finite-difference schemes, as high-order differencing approximations greater than the second order are more difficult to develop in 3D. This is due to the two levels of approximation: interpolation and integration. Despite this drawback, this method is quite advantageous. [10]

Chapter 3

MYRRHA

Due to the complexity of the reactor, in this chapter, a general approach of the MYRRHA project for further understanding is made. MYRRHA stands for: **M**ulti-purpose h**Y**brid **R**esearch **R**eactor for **H**igh-tech **A**pplications.

3.1 Applications

This project proposes to achieve the following applications:

- Demonstrate the ADS full concept while combining the three components (accelerator, spallation target and sub-critical reactor) at reasonable power level in order to obtain operation response, extensible to an industrial demonstrator

- To study the efficiency of the P&T technology of high level nuclear waste

- To be operated as a flexible fast spectrum irradiation facility while permitting:

  - Fuel developments for innovative reactor systems, being the main target the fast spectrum GEN IV systems, which require fast spectrum conditions
  - Material developments for GEN IV systems
  - Material developments for fusion reactors
  - Radioisotope production for medical and industrial purposes

3.2 Design

The MYRRHA facility consists of [11]:

- The reactor building, containing two systems: the primary and the secondary systems

- Tertiary system

- The accelerator building and beam line, containing the accelerator

- Other supporting buildings.

An overview of each part is made in the following subsections.

Primary System

The primary system consists of a pool type reactor cooled by liquid LBE, contained inside the reactor vessel and the reactor cover. This system consists of all the primary equipment: pumps, heat exchangers, fuel handling tools, experimental rigs, etc.) The diaphragm separates the hot and cold LBE, supports the In-vessel Fuel Storage and provides a pressure separation. The core barrel and the core support plate constitute the core support structure, which holds in place the core.

Secondary System

This system consists of a water-cooling system. It may function in active mode during normal operation, or in active or passive mode for decay heat removal.

Tertiary System

Likewise the secondary system, this system can function in both active and passive mode for decay heat removal, although its full power operation is always active. However, unequally to the secondary system, this system is cooled by air. Its position is yet to be determined.

Accelerator building and beam line

MYRRHA-FASTEF is capable of operating in both ADS and critical mode. While operating in critical mode, higher power levels may be achieved and a larger core is also allowed. However, control rods and safety rods are a requirement in the critical core mode.

Accelerator driven systems (ADS) are subcritical (i.e. $k_{eff} < 1$) core nuclear fission reactors that require an external neutron source in order to have a stable neutron economy in the core. In the case of MYRRHA, for an initial medium-scale ADS, a sub-criticality level of around 0.95 was considered, which is the level criticality accepted by the safety authorities.

The role of the heavy liquid metal is to act as a spallation target. The protons accelerated to 600 MeV from the proton linear accelerator hit the heavy liquid metal and produce the neutrons, which sustain the chain reaction in the subcritical core. The current of the protons depends on the reactor power. This building is part of the main building layout.

An example of a successful ADS development is the MEGAPIE spallation neutron target, tested at the SINQ facility of the Paul Scherrer Institute in Switzerland[12].

3.3   Design characteristics

Since the centre offers limited space, a compact core is needed and, consequently, the hole in the core where the spallation target is stored should be of limited dimensions. The choice of the fuel MOX was based on the considerable experience in Europe, notably in Belgium, with a maximum plutonium enrichment of 35%.

The components of the primary loop are inserted in a pool type system from the top in penetrations in the cover, benefiting from the thermal inertia caused by a large coolant volume. Dissimilarly, the loading of fuel assemblies is predicted to be form underneath. This was thought to take advantage of the buoyancy force in the LBE. In addition, it also allows keeping a large flexibility for the experimental devices inserted from the top.

For corrosion prevention purposes, while controlling the oxygen in the LBE, the pool vessel is placed in an oxygen deficient containment environment. It was set that the design of both operation and maintenance (O&M) and In-service Inspection and repair (ISI&R) of MYRRHA was to be made with fully remote handling systems. This was based on several factors, like:

- High availability rate desired (65 to 75%)

- High activation on the top of the reactor (due to neutron leakage through the beam line)

- The polonium (Po) contamination when extracting components (due to the existence of bismuth in the LBE)

- The non visibility under LBE

- The oxygen free atmosphere in the reactor's hall

3.4 Power level

The difference between operating in ADS mode and critical mode resides in the possible highest power that can be applied. The maximum power depends on the maximum cladding temperature of the hottest pin as well as the maximum LBE flow velocity. According to the current design, the maximum power for ADS mode and critical mode is of 60 MW and 72 MW, respectively. Taking into account conceivable future power increases, the components of MYRRHA are designed for a maximum 100 MW.

3.5 Operational cycle

The normal operating cycle of the system is programmed to last 90 days, followed by a period of 30-day maintenance. Every third cycle, it goes through a long maintenance phase of 90 days. This was planned in contemplation of an availability of 65%.

3.6 Geometry

In this section, a descritpiton of each component of the geometry of the MYRRHA reactor is made. However, it is important to point out that it has been evolving throughout the years. The geometry considered for this work is the version 1.6, whilst in the comparative document [4] it is the version 1.4. It is also relevant to note that given the fact that some areas of the geometry are very dense, porous media (described in 3.6.1) was applied in these same areas. In figures 3.1 and 3.2, the full geometry of the reactor is presented whilte in figure 3.3, the inside components of the reactor are shown.

3.6.1 Porous Media

The porosity is defined as the ratio between the volume of the fluid and the total volume of the media, and it's represented by γ. It characterizes each porous zone and is used in the prediction of heat transfer in the porous media.

Darcy's law (1856) links pressure drop and velocity in fluid flow through porous media. However, as velocities increase, a difference between experimental data and results obtained for Darcy's law appears. This way, Darcy-Forcheimmer was obtained to link this discrepancy to inertial effects. Forcheimmer (1901) suggested to add a term to Darcy's law representing kinetic energy [13].

$$-\frac{\Delta p}{L} = \frac{1}{\omega}(\mu \overrightarrow{u}) + \beta(\rho \overrightarrow{u^2}) \tag{3.1}$$

where:

- Δp – pressure drop
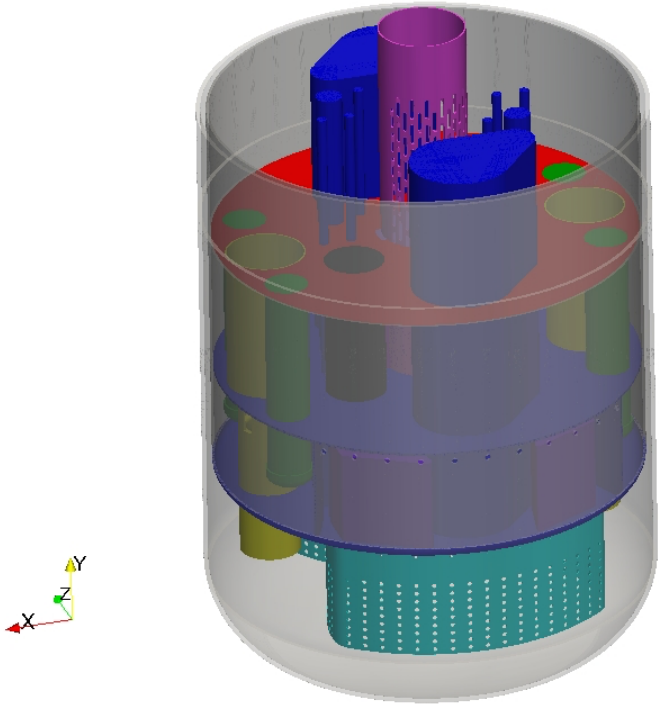
Figure 3.1: Full geometry of MYRRHA reactor
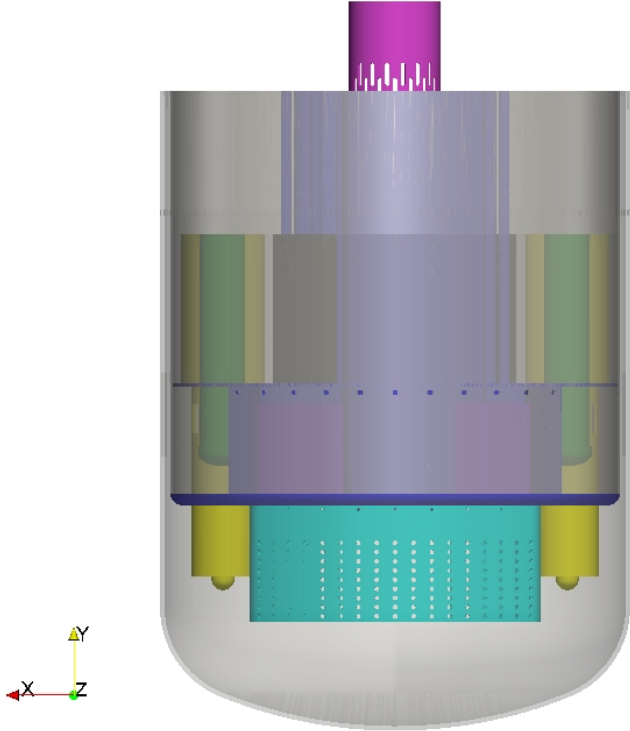
Figure 3.2: Side perspective

- L – reference length (m)

- ω - permeability coefficient (m^2)

- β - Forchheimer coefficient (m^{-1})
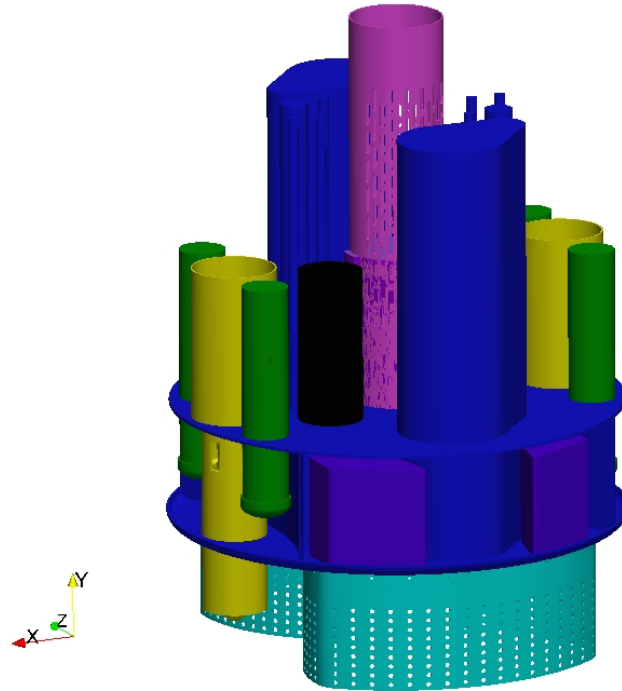
Figure 3.3: Inside components of the reactor

- u - velocity (m/s)

An additional flow resistance which takes a form of a source of mass forces is considered and is added to the source term of momentum balance equation.

The resultant standard equation as a momentum sink when adding the pressure losses caused by friction has two terms: one described by Darcy's law, corresponding to losses due to viscosity, and the second one described by Forchheimer's law, taking into account losses due to viscosity and inertia. Therefore, according to OpenFOAM's porous media model, also used in ANSYS-Fluent, [13] [14], this equation is as follows:

$$S = -(\mu d u + \frac{1}{2}\rho\beta u^2) \tag{3.2}$$

Where:

- d - Darcy coefficient (m^{-2})

The viscous losses are not considered, only the inertial resistance (second term of **??** and **??**). Once the expected pressure drop is known, the inertial resistance coefficient can be calculated according to the estimated flow rate:

$$C_2 = \frac{\triangle p_{porous}}{L_{ref}\dfrac{p}{2} - \tilde{u}^2} \tag{3.3}$$

Where:

- ũ – superficial velocity

The Darcy-Forcheimmer law was implemented to module the porous media in the HX, in certain layers of the core and in the ACS.

3.6.2 Pumps

The pumps drive the flow field within the reactor. These are two HX/Pump casing, each one containing two HX and one pump.

The previous studies performed showed that the effect of the swirl created by the blades can be disregarded, as it does not influence parameters of interest for this study, for example pressure drops. Modelling the flow through the rotor would require meshing around the blades and modelling their dynamic behaviour. Moreover, this study only concerns the nominal flow conditions of the primary coolant loop. Consequently, the presence of the rotor can be neglected in the CFD model.

Two approaches to represent the primary coolant are possible: either an open system or a closed system. On 3.4 the geometry of the pumps can be seen.

In the first approach, the rotor area (annular volume between red and green ring) is neglected in the CFD model and the nominal mass flow rate (most important parameter of MYRRHA) is imposed at the pump's outlet (green surface) with a value of 9440 kg/s under nominal conditions, while velocity conditions are detailed. Then, pressure is imposed at the pump's inlet (red surface). In order to impose a certain amount of swirl to the flow, a tangential velocity component can be specified at the outlet.
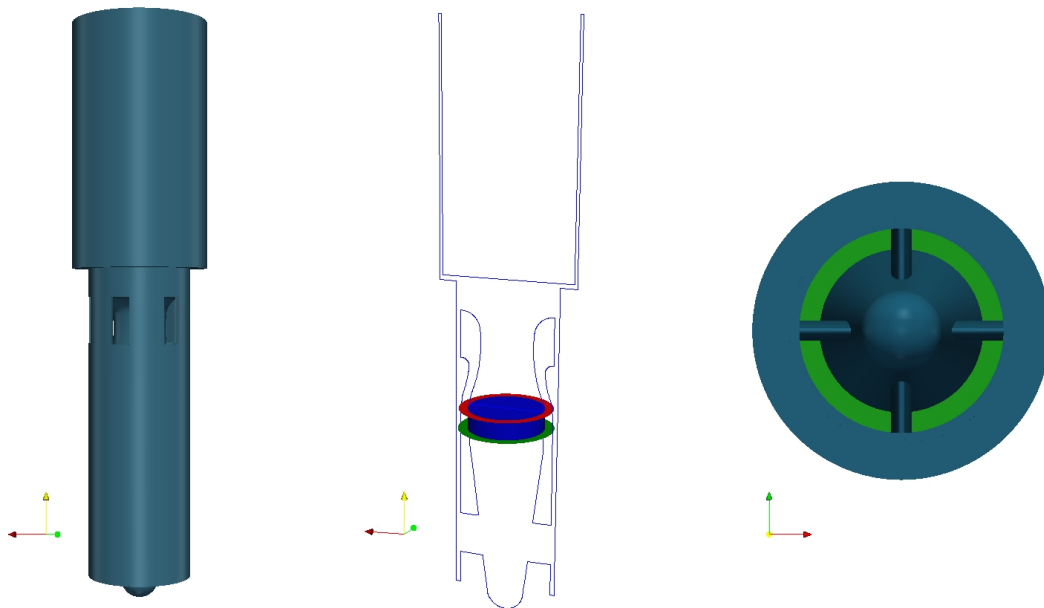
Figure 3.4: Pump inlet (red) and outlet (green) surfaces

Nevertheless, in transient simulations (for example pump failure), a closed-loop system is the simplest way of insuring that the flow between the pump's inlet and outlet is continuous. In order to balance the chosen mass flow rate, the flow motion is later activated by a momentum source applied to the rotor area and fixed. The balance between the inlet and outlet is given by:

$$\dot{m}(\overline{u}_b - \overline{u}_a) = p_a S_a - p_b S_b + F_m + G + \mathcal{V} \tag{3.4}$$

With:

- G – gravity term

- $\mathcal{V}$ – viscous term

- F_m – momentum source

Computing the momentum source is important to balance the pressure difference in the volume. This pump head compensates the natural pressure drops (through extensions, contractions, holes…) and the pressure losses due to the porous media. However, the source should then be adjusted to provide the right mass flow rate.

3.6.3   Butterfly

The objective of the butterfly, or baffle, is to avoid any fuel element (FA) to get out of reach of the in-vessel fuel handling machine (IVFHM). It is located in the lower plenum. It has holes in its structure, in order to mix the flow in the lower plenum (42 of 5 cm diameter in the upper part and 774 of 8 cm diameter in the lower part).

The butterfly was not modelled as porous media as it would increase the mesh size and the flow passing through the holes is perpendicular to the shell. Due to its shape it is difficult to define a local reference coordinate system, and therefore it is not possible to set a very high tangential inertial resistance coefficient.
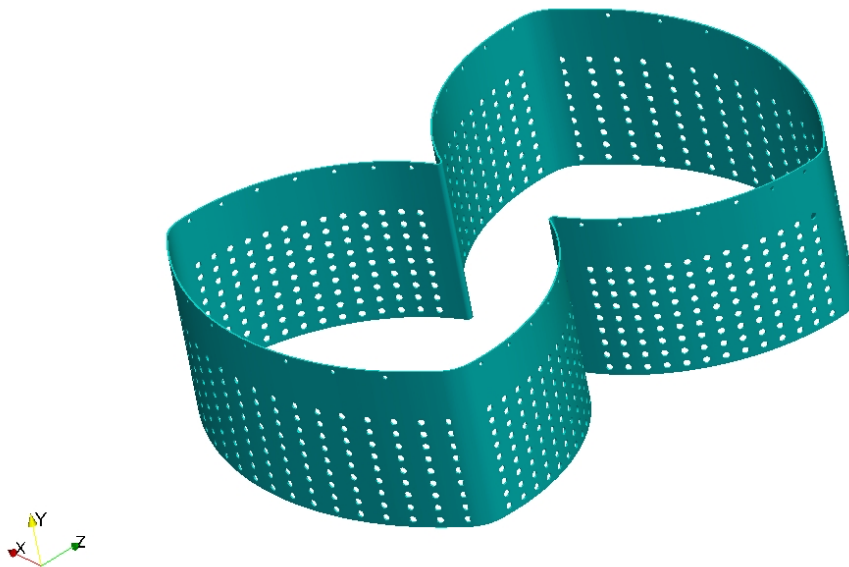
Figure 3.5: Butterfly

3.6.4   Core

This component has been modelled as a porous media. It is composed by:

- The central core, which consists of 5 porous rings with a height of 1.78 m, from the centre: the inner FA, combination of IPS+SR+CR, the outer FA, the inner dummies and the outer dummies.

- The area directly below the core: grid with cones that hold the FA in place. This grid makes the connection with the CRS (core restraint system). This area is considered as non-porous due to the small flow blockage from both axial and radial directions.

- The combination of IPS, SR and CR can be approximated as a single ring since these components are arranged separately between the FA, and therefore this is a non-negligible assumption momentum and heat transfer wise.

In 3.6 a) we can see the layers of the core modelled with the porous media approach. In 3.6 b) all the layers of the core are shown, as well as in 3.6 c) but with opacity.
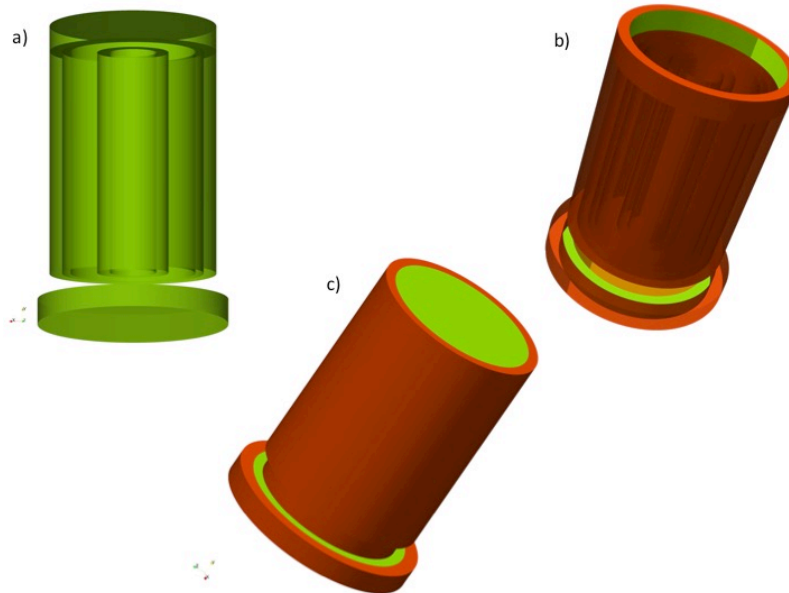
Figure 3.6: Core
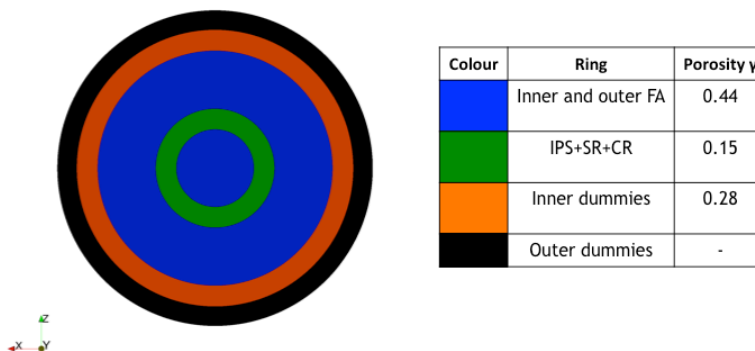
Figure 3.7: Distribution of porosity in core layers

Colour	Ring	Porosity γ
	Inner and outer FA	0.44
	IPS+SR+CR	0.15
	Inner dummies	0.28
	Outer dummies	-

In 3.7 the layers are represented in different colours, according to its porosity. The outer ring (in black) is a solid component, therefore not considered in the porous domain. It is referred to as core jacket and is the structural interface between outer hexagonal fuel assemblies and the round core barrel. It maintains the core geometry and acts as radiation shielding, protecting the core barrel. As mentioned in 3.6.1, the Rehme correlation was used to calculate the expected

pressure drop in the core.

It can be considered that an uniform pressure drop of 1.7 bar is expected in the core, despite the different porosity and mass flow rates in some of the central core rings. From the lower plenum up to the free surface (radial losses through the barrel holes included) the pressure drop is estimated to be around 2 bar.

The superficial velocity is calculated by multiplying the real velocity by the media's porosity. In conclusion, each porous media is defined by the γ value and by the inertial resistant coefficient ($C_{2,r}$,$C_{2,y}$) in the radial and axial direction, respectively.

The value of $C_{2,r}$ is assumed to be high (1000 m^{-1}) in the core region as the flow is blocked in the radial direction, given the presence of various instrumentation tubes and guiding vanes. The cross sections of the rings are determined according to the fractions of core positions take. When working in critical configuration, the core of MYRRHA consists of 69 fuel assemblies, 24 inner dummies, 42 outer dummies, 3 SR, 6 CR and 7 IPS. Then, it is possible to determine the mass flow rate distribution based on these cross sectional areas and a nominal total mass flow rate of 9440.4 kg/s. In the following table 3.1 the expected mass flow distribution is presented:

Table 3.1: Theoretical mass flow rate distribution in the core

Core ring	Theoretical distribution (kg/s)
FA	5186
IPS+SR+CR	350
Inner dummies	1804
Outer dummies	2100
Total	9440

In normal operation, the pressure drop is determined according to the pressure drop in the FA. By recurring to the Rehme correlation for a fuel bundle as a function of the local Reynolds number, f(Re), it is possible to estimate the value of the pressure drop:

$$\triangle P = f \frac{L_{pin}}{D_{eq}} 0.5 \rho u^2 \tag{3.5}$$

where:

- u – local flow velocity

- L_{pin} – pin length

- D_{eq} – equivalent diameter

- f – friction factor

The friction factor is given by:

$$f = \left(\frac{64}{Re} F^{0.5} + \frac{0.0816}{Re^{0.133}} F^{0.9335} \right) N_r \pi (D_r + D_w) \frac{1}{St} \tag{3.6}$$

With:

- N_r - number of pins

- D_r – clad outside diameter

- D_w – wire diameter

- F – geometrical factor

- St - Stanton number

The geometrical factor value is of 1.225. For the FA inner core, outer core and for the core inner dummies, the Re and f are calculated by recurring to the previous equations, implemented within the numerical model. The inner dummies are modelled as the FA rings since these have the same flow rate and pressure drop.

With respect to the IPS+SR+CR and core outer dummies, the axial resistance was kept constant and first approximated with base on the desired mass flow rate distribution, from which an average LBE velocity can be extracted, being the values adjusted to be more approximated to the distribution.

In the case of the core support plate (CSP) and the CRS regions, the axial resistance coefficient was calculated in order to reach a total pressure drop of 2 bars across the whole central region of the reactor. A summary of the final porous media parameters can be found in the following table 3.2

Table 3.2: Porous media parameters in the core

Porous zone	Porosity γ	Axial resistance $C_{2,y}$ (m^{-1})
CSP	0.15	24
Core inner FA	0.44	f(Re)
Core IPS+SR+CR	0.15	374
Core outer FA	0.44	f(Re)
Core inner dummies	0.44	f(Re)
Core outer dummies	0.28	74
CRS	0.15	67

3.6.5   Core heat source distribution

The heat in the core is modelled as a volumetric heat source of 100 MW in total and is limited to the inner and outer FA rings, where the nuclear reaction is noteworth. The foreseen radial power distribution , which can be seen in 3.8, is approximated by a third order polynomial to approach an integrated power of 24.6 MW and 75.4 MW in the inner and outer FA rings.
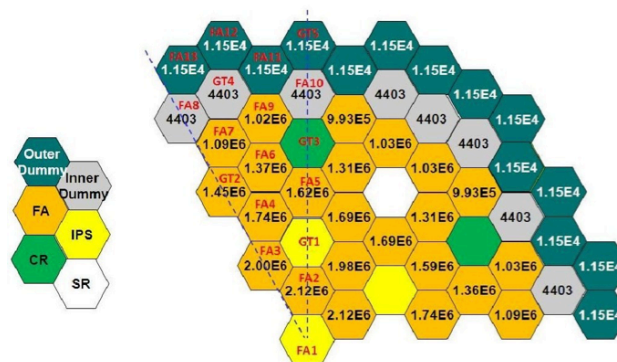
Figure 3.8: Radial power distribution in the MYRRHA reactor core

The final expression used to model the core heat source distribution is given in W/m^3 by:

$$Q_{core}(r,y) = 1.86 \cos\left(\frac{\pi}{1.78}(y + 0.29)\right)(309.45r^3 - 637.4r^2 + 9.13r + 214.8) \tag{3.7}$$

3.6.6   Barrel

Located in the centre of the reactor, the barrel is an integral part of the core support structrue, CSS. Its function is to guide the LBE flow from the lower (cold) plenum to the upper (hot) plenum through several holes which allow the hot LBE originating from the core flow into the upper plenum. The ACS (Above core structure) contains a number of guide tubes and instrumentation tubes and is surrounded by the upper part of the barrel.
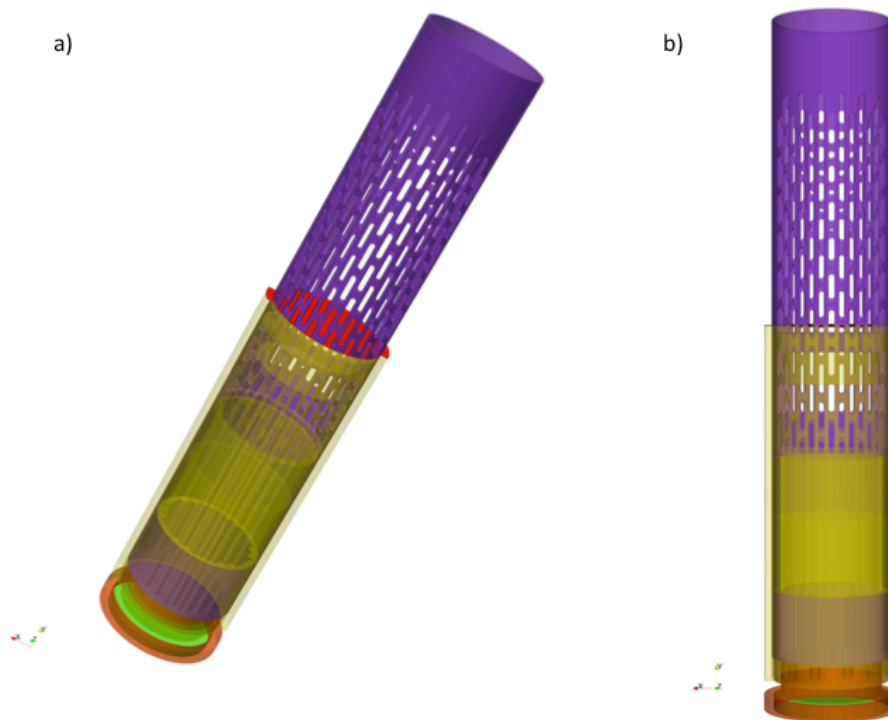
Figure 3.9: Barrel

Two chinmeys that contain the actuating rods are located on the sides of the barrel, as seen in figure 3.10. Their purpose is to lower the CRS and are neglected from the CFD model as they are considered solid zones. The free surfaces are shown in green and the hot plenum in orange in 3.10.

The top and lower part of the ACS are modelled with the porous media approach, with a porosity of 1. The inertial resistance coefficient is set to 2 m^{-1} in the axial direction while the radial flow blockage is imposed to be $C_{2,r} = 1000$ m^{-1} From the free level of LBE to just above the outlet nozzles of the fuel assemblies, the ACS is also modelled as a porous media. Derivation of porous media properties of the ACS were based on the book [15].

3.6.7   Free surfaces

Regarding the free surfaces, some assumptions are made. The LBE free-surfaces are approached by a free slip condition and modelled as zero shear slip walls since their level is not expected to vary much, given the steady-state nature of the problem.
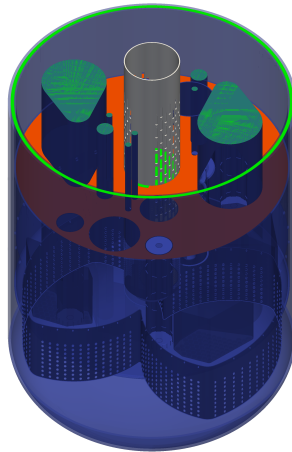
Figure 3.10: Hot plenum and barrel free surfaces

3.6.8   Primary Heat Exchanger

Once the heat is collected from the nuclear reaction, the pumps aspirate the existing hot LBE in the hot plenum into the four heat exchangers (HX). In the heat exchangers, the heat is transferred to the secondary coolant, consisting of a mixture of liquid and steam water like in most nuclear power plants. Consequently, the cooled LBE exits the HX's and is sucked into the pumps and expelled at a higher pressure into the cold plenum.
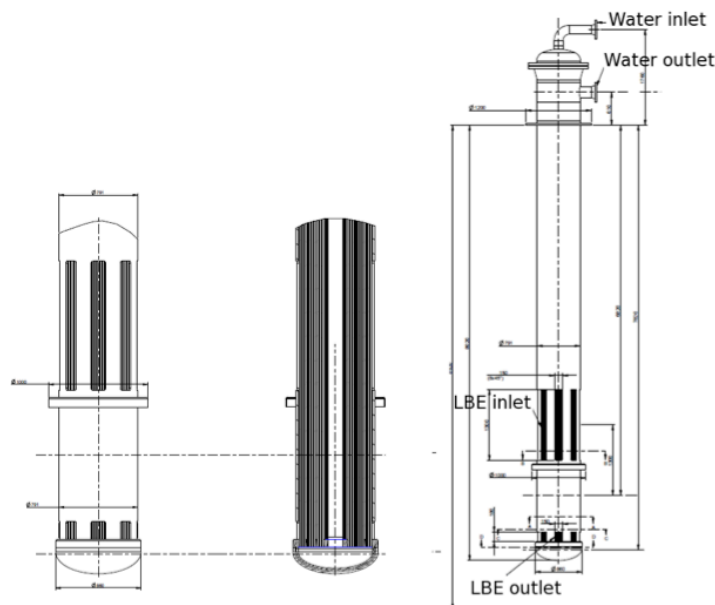
Figure 3.11: Primary Heat Exchanger scheme

In 3.11 we can see the design of the FASTEF HX. The LBE flows outside the water tubes downwards, while the two-phase water flows upwards. During normal operation, one of the HX's main functional requirements is to remove the power generated by the reactor core and all of the other sources. Taking these requirements into account, it is designed to extract 110% of the

nominal core power. In conclusion, the number and dimensions of the water tubes achieved to be enough for the HX to extract 27.5 MW is of 684 water tubes with an external diameter of 16 mm.

To avoid representing the numerous water tubes in the CFD model, the HX is simplified by using the porous media approach, which can be seen in green in figure 3.12 occupying all the volume of the HX. Its upper part is limited by the LBE free surface level.
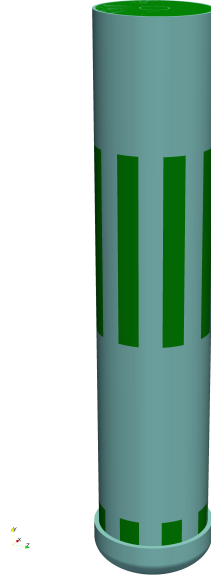
Figure 3.12: Primary Heat Exchanger

Therefore, the only represented tube is the feed water pipe in the centre, subtracted from the numerical domain. The porosity is calculated with base on the cross-sectional area of the feed water pipe and the smaller water tubes. The pressure drop is obtained with the theoretical average velocity, and therefore the inertial resistance coefficient is calculated. The values for the porous media definition in the HX can be found in the following table 3.3:

Table 3.3: Porous media parameters in the HX

Porous zone	Porosity γ	Axial resistance $C_{2,y}$ (m^{-1})	Radial resistance $C_{2,x}$ (m^{-1})
HX	0.62	1.55	0.32

The heat transfer between the primary and secondary coolant is represented in the CFD model by a variable heat sink positioned in the HX porous zone.

To obtain the Nusselt number (Nu), the following correlation derived by P.A Ushakov (1977) for the flow of a liquid metal in triangular or hexagonal rod bundles arrays [16] with a pitch-to-diameter ratio (P/D) between 1.3 and 2.0 and Peclet numbers between 1 and 4000 [17] and constant q_w is applied:

$$Nu = 7.55 \left(\frac{P}{D}\right) - 20 \left(\frac{P}{D}\right)^{-13} + \frac{3.67}{90(P/D)^2} Pe^{\left(0.19\left(\frac{P}{D}\right)+0.56\right)} \tag{3.8}$$

where P/D is the pitch-to-diameter ratio and Pe is the Peclet number given by:

$$Pe = Re \cdot Pr \tag{3.9}$$

with

$$Re = \frac{\rho \, u_{magn} \, D_H}{\mu} \qquad Pr = \frac{\mu C_P}{\lambda} \tag{3.10}$$

where:

- ρ - density of the fluid (kg/m^3)

- u_{magn} - velocity magnitude

- D_H - hydraulic diameter of the pipe (m), $D_H = \dfrac{4A}{P}$ where A is the cross-sectional area and P is the wetted perimeter

- μ - dynamic viscosity of the fluid (Pa·s = N·s/m^2 = kg/(m·s))

- C_p - specific heat (J kg^{-1}K^{-1})

- λ - thermal conductivity (W/m.K)

In the simulation, the local velocity magnitude u_{magn} is considered to calculate the local heat transfer described by Nu. The latter is then used to determine the heat transfer coefficient h_e on the LBE side, given by:

$$h_e = \frac{Nu\lambda}{D_H} \tag{3.11}$$

Now we can finally obtain the total local heat transfer U, while considering the water tube's heat transfer resistance R and the heat transfer coefficient h_i on the waterside:

$$U = \frac{1}{\left(\dfrac{1}{h_e} + R + \dfrac{1}{h_i}\right)} \tag{3.12}$$

To obtain the volumetric heat sink S_{PHX} in the core, the following equation is used:

$$S_{PHX} = \frac{U A_{exchange}(T - T_{water})}{V_{PHX} \cdot F_{PHX}} \tag{3.13}$$

With:

- $A_{exchange}$ - water tubes' exchange surface

- V_{HX} - HX's Volume

- $T - T_{water}$ - local temperature difference between the LBE and the water

- F_{HX} - factor to adjust the heat that is removed

The water temperature is considered to be 473.15 K (200 ℃). F_{HX} is fixed to 0.52 so that around 25.5 MW are removed by each HX when heat losses are neglected.

3.6.9   Diaphragm

The diaphragm's function is to separate the cold low pressure LBE from the hot high pressure LBE, therefore it separates the cold and hot plenum. It is composed by three different volumes: central volume surrounding the core, the volume surrounding the IVFS and the volume of the pump boxes. It incorporates two horizontal plates connected by vertical shells and tubes and with seeveral volumes in between. Two of these volumes house the pumps and the PHX. The connecting tubes, called chimneys, are the penetrations for the components which have to

access the cold plenum. The low pressure cold LBE originating from the PHX is aspired by the primary pump into the pump boxes, therefore separating the stresses between the lower plate and the upper plate, induced by the pressure difference and thermal gradient. In figure 3.13 the diaphgram can be seen in red and the main walls in green.
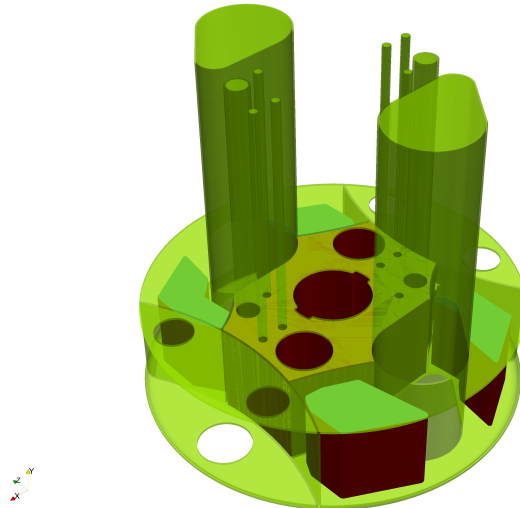
Figure 3.13: Diaphgram

3.6.9.1   IVFS

Four racks, each capable of storing half a core, with 76 positions to place the Fuel Assemblies, compose the In Vessel Fuel Storage. In the CFD model, the different individual positions are represented with the porous media approach (as mentioned in 3.6.1, surrounding all the storing positions. The FA are inserted in the pipes of the IVFS and prevail until their residual heat has sufficiently decayed. It is assumed that all racks are fully occupied by the FA. Therefore, the same parameters are considered for both IVFS and FA rings porous media, as specified in section 3.6.1. The stored FA release some residual heat, making the IVFS an additional source of energy. Therefore, each FA has a uniform heat source in order to inject an extra 2MW in total. The loading and unloading of the assemblies to the IVFS is handled by two in-vessel fuel-handling machines, installed permanently in the reactor. Natural convection is also present, as the LBE is able to flow within the IVFS, contributing to cool down the FA. For this purpose, numerous holes are located in the cylindrical shell of the inner vessel, between the two plates of the IVFS casing. The IVFS was modelled with the Rehme Correlation and with a porosity of 0.44. The following figure 3.14 shows the porous media (IVFS) of the diaphgram in blue.

3.7   Primary coolant: Lead-Bismuth Eutectic

This section presents an overview of the primary coolant of the reactor.

The choice of a liquid metal as a primary coolant was based on the aim to obtain a high fast
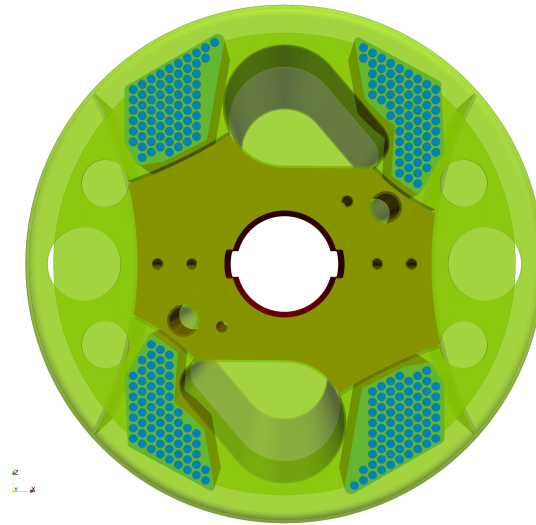
Figure 3.14: IVFS

flux, high power density and short deployment of MYRRHA (start before 2020). Gaseous coolants were not an option because gases have a lower density in relation to liquids and therefore poor heat transfer characteristics, which is non-desirable for a fast reactor [18].

In a flexible irradiation facility like MYRRHA, fire safety risks have to be carefully taken into account. Therefore, sodium was not elected as coolant due to its chemical reactivity with water and air. Given these restrictions, the alternative liquid metals are lead (Pb) and lead-bismuth eutectic (LBE), currently considered the potential candidates for the coolant of new generation fast spectrum nuclear reactors and ADS and for liquid spallation neutron sources (Sobolev, 2012). However, these coolants present the disadvantage of having a high corrosion rate of steels at high temperatures (>773 K). To avoid corrosion problems it is desirable that the primary systems function at low temperatures. Since the LBE presents a low melting temperature (398 K) while lead has a higher melting temperature (600 K), it allows low operation temperature range resulting in lower corrosion rates and in easier maintenance, and was therefore the chosen option.

Metals and the other media differ mainly because metals have a significantly higher thermal conductivity λ [W m^{-1}K^{-1}] and lower specific heat capacity c_p [J kg^{-1} K^{-1}]. For the same velocity, LBE presents larger Re, because its kinematic viscosity ν [m^2 s^{-1}] is often smaller than that of air or water. Combining all these properties, we can obtain a characteristic dimensionless quantity, the Prandtl number Pr. Physically, the Prandtl number weights the transport coefficients of momentum (ν) and thermal energy (α) and is therefore a fundamental parameter to take into account in convective heat transfer problems. It is important to note that this parameter depends only on the physical properties of the fluid, being independent of the velocity or the geometry. It is defined as the ratio of momentum diffusivity to thermal diffusivity in a fluid:

$$Pr = \frac{c_p \mu}{\lambda} = \frac{\nu}{\alpha} \quad where \quad \alpha = \frac{\lambda}{\rho} c_p \tag{3.14}$$

The LBE presents a low Prandtl number, meaning that the thermal diffusivity dominates and that its material properties are highly dependant on temperature Liquid metals present Prandtl

numbers in a lower range: $0.002 \leq \text{Pr} \leq 0.06$.

Nevertheless, LBE has some disadvantages. Due to the existence of bismuth, radioactive capture of neutrons occurs, leading to the production of the alpha-active polonium. Still, it is the best option between the liquid metals, since the other alloys of lead without bismuth require very low oxygen content in coolant and their properties are not yet very well known [12].

3.7.1 Properties

Linear or second order interpolation of experimental data collected in the database for liquid LBE returns for the LBE density ρ_{LBE}, conductivity λ_{LBE} and heat capacity $C_{P_{LBE}}$:

$$\rho_{LBE} = 11096 - 1.3236\,T \tag{3.15}$$

$$\lambda_{LBE} = 3.61 + 1.517 \times 10^{-2}\,T - 1.741 \times 10^{-6}\,T^2 \tag{3.16}$$

$$C_{P_{LBE}} = 159 - 2.72 \times 10^{-2}\,T + 7.12 \times 10^{-6}\,T^2 \tag{3.17}$$

As for dynamic viscosity μ_{LBE}, the viscosity database yields the following correlation:

$$\mu_{LBE} = 4.94 \times 10^{-4} e^{754.1/T} \tag{3.18}$$

These equations were implemented within myrrhaSimpleFoam in the file related to the properties of the LBE. In the isothermal scenario, the density and the dynamic viscosity are fixed to $\rho_{LBE} = 10377.1$ kg/m^3 and $\mu_{LBE} = 0.00198 Pa.s$.

Chapter 4

Numerical set up

In this chapter, the numerical characteristics and set up of the simulation are exposed. The present work considers a steady-case of an incompressible turbulent flow.

A flow with constant velocity, pressure, density, etc., at any position and that does not change with time, is a steady flow [19].

A turbulent flow is characterized by chaotic changes in pressure and flow velocity. Amongst others, it has the following characteristics:

- Irregularity: therefore turbulent flows are analysed statistically

- Diffusivity: the enhanced mixing and increased rates of mass, momentum and energy transports that characterizes turbulent flows.

- Near walls, since they are solids, the flow has a distinct structure called boundary layer. Here, the velocity of the fluid decreases to zero, so we can see the "no-slip" condition, i.e, the fluid velocity is the same as the boundary velocity and therefore has no relative slip. This is due to viscosity, ν, which is a fluid's resistance to flowing or fluid friction. The higher the viscosity, the more the fluid resists to flowing.

4.1 Reynolds Decomposition

The Reynolds decomposition decomposes the flow property φ in a steady mean component ϕ and a time varying fluctuating component $\varphi'(t)$ with zero mean value, so we obtain:

$$\varphi(t) = \phi + \varphi'(t) \tag{4.1}$$

Turbulent eddies originate fluctuations in velocity. In turbulent flow, the velocity record is decomposed in both a mean and a turbulent component, i.e, instantaneous quantity is decomposed into its time-averaged and fluctuating quantities [20].

$$u(t) = \overline{u} + u'(t) \qquad v(t) = \overline{v} + v'(t) \tag{4.2}$$

Where u is the longitudinal velocity and v is the vertical velocity, both varying in time due to turbulent fluctuations.

Due to the random nature of eddies, a statistical approach to the turbulent motions can be done. Theoretically, the velocity record is continuous and the mean can be evaluated through integration. Nonetheless, in practice the measured velocity records are a series of discrete points, u_i. The mean velocity

$$\overline{u} = \int_t^{t+T} u(t)dt = \frac{1}{N}\sum_1^N u_i \tag{4.3}$$

where, time T is much longer than any turbulence time scale, but much shorter than the time-scale for mean flow unsteadiness. The turbulent fluctuations are given by:

- Continuous record: $u'(t) = u(t) - \overline{u}$

- Discrete points: $u'_i = u_i - \overline{u}$

The turbulence strength, which is considered to be the standard deviation u_{rms} of the set of random velocity fluctuations u'_i, is given by:

$$u_{rms} = \sqrt{\overline{u'(t)^2}} = \sqrt{\frac{1}{N}\sum_{i=1}^{N} u'^2_i} \tag{4.4}$$

where the subscript *rms* stands for root-mean-square.
The higher u_{rms}, the higher the level of turbulence. Another consideration to take into account is that shear produces turbulence, and, the stronger the shear, the stronger the turbulence.

4.2   Numerical methods

Turbulence originates eddies with a wide range of length and time scales, interacting in a dynamically complex way. Therefore, it is important to capture the effects of turbulence in the flow. For that purpose, three categories of numerical methods exist:

- Turbulence models for Reynolds-averaged Navier-Stokes (RANS) equations

- Large eddie simulation (LES)

- Direct numerical simulation (DNS)

For this study case, the RANS approach is used, as it requires modest computing resources for reasonably accurate flow computations. An overview of this method is made in the following sub-section 4.2.1.

4.2.1   Reynolds-averaged Navier-Stokes equations

The following instantaneous continuity equation and Cartesian co-ordinate system of equations governs every turbulent flow for the velocity vector u. The vector has the component-x u, component-y v and component-z w:

$$\text{div } \mathbf{u} = 0 \tag{4.5}$$

$$\frac{\partial u}{\partial t} + \text{div}(u\,\mathbf{u}) = -\frac{1}{\rho}\frac{\partial p}{\partial x} + \nu\,\text{div}\,(\text{grad}(u)) \tag{4.6}$$

$$\frac{\partial v}{\partial t} + \text{div}(v\,\mathbf{u}) = -\frac{1}{\rho}\frac{\partial p}{\partial y} + \nu\,\text{div}\,(\text{grad}(v)) \tag{4.7}$$

$$\frac{\partial w}{\partial t} + \text{div}(w\,\mathbf{u}) = -\frac{1}{\rho}\frac{\partial p}{\partial z} + \nu\,\text{div}\,(\text{grad}(w)) \tag{4.8}$$

With the effects of fluctuations on the mean flow, using the Reynolds decomposition in the previous equations and replacing the flow variables u and p by the sum of a mean and a fluctuating component, we obtain:

$$\mathbf{u} = \mathbf{U} + \mathbf{u'} \quad u = U + u' \quad v = V + v' \quad w = W + w' \quad p = P + p' \tag{4.9}$$

Considering the continuity equation and taking the time average, first:

$$\text{div } \mathbf{u} = \text{div } \mathbf{U} \tag{4.10}$$

And thus we have the continuity equation for the mean flow, where U is the velocity steady mean value:

$$\text{div } \mathbf{U} = 0 \tag{4.11}$$

The Navier-Stokes equations are time averaged before a numerical method is applied. Rewriting the time averages of the individual terms in the x-momentum equation we obtain:

$$\frac{\partial u}{\partial t} = \frac{\partial U}{\partial t} \qquad \overline{\text{div}(u\mathbf{u})} = \text{div}(U\mathbf{U}) + \text{div}(\overline{u'\mathbf{u'}}) \tag{4.12}$$

$$\overline{-\frac{1}{\rho}\frac{\partial p}{\partial x}} = -\frac{1}{\rho}\frac{\partial P}{\partial x} \qquad \overline{\nu \text{ div}(\text{grad}(u))} = \nu \text{ div}(\text{grad}(U)) \tag{4.13}$$

Substitution of these terms gives the time-average x-momentum equation:

$$\frac{\partial U}{\partial t} + \text{div}(U\mathbf{U}) + \text{div}(\overline{u'\mathbf{u'}}) = -\frac{1}{\rho} + \nu \text{ div}(\text{grad}(U)) \tag{4.14}$$

The same applies for the y- and z-momentum equations. We can verify that due to the process of time averaging, a new term that was not in the instantaneous equations appears: $\text{div}(\overline{u'\mathbf{u'}})$. This term consists of products of fluctuating velocities and are associated with convective momentum transfer due to turbulent eddies [5].

In conclusion, we obtain the Reynolds-averaged Navier-Stokes equations, where the new terms are placed on the right hand side of the equations to highlight their role as additional turbulent stresses on the mean velocity components U, V and W:

$$\frac{\partial U}{\partial t} + \text{div}(U\mathbf{U}) = -\frac{1}{\rho}\frac{\partial P}{\partial x} + \nu \text{ div}(\text{grad}(U)) + \frac{1}{\rho}\left[\frac{\partial(-\rho\overline{u'^2})}{\partial x} + \frac{\partial(-\rho\overline{u'v'})}{\partial y} + \frac{\partial(-\rho\overline{u'w'})}{\partial z}\right] \tag{4.15}$$

$$\frac{\partial V}{\partial t} + \text{div}(V\mathbf{U}) = -\frac{1}{\rho}\frac{\partial P}{\partial y} + \nu \text{ div}(\text{grad}(V)) + \frac{1}{\rho}\left[\frac{\partial(-\rho\overline{u'v'})}{\partial x} + \frac{\partial(-\rho\overline{v'^2})}{\partial y} + \frac{\partial(-\rho\overline{v'w'})}{\partial z}\right] \tag{4.16}$$

$$\frac{\partial W}{\partial t} + \text{div}(W\mathbf{U}) = -\frac{1}{\rho}\frac{\partial P}{\partial z} + \nu \text{ div}(\text{grad}(W)) + \frac{1}{\rho}\left[\frac{\partial(-\rho\overline{u'w'})}{\partial x} + \frac{\partial(-\rho\overline{v'w'})}{\partial y} + \frac{\partial(-\rho\overline{w'^2})}{\partial z}\right] \tag{4.17}$$

These equations represent the transport equations for the mean flow variables and the effects of turbulence on mean flow properties, reducing the computational effort. Since the mean flow is steady, time derivatives disappear. To model the extra terms that appear due to the interaction between turbulence fluctuations, classical turbulence models are used (like the $\kappa - \varepsilon$ model and the Reynolds stress model), as these allow predicting the Reynolds stresses and the scalar transport terms and close the system of mean flow equations.

4.2.2   RANS Temperature Equation

To model turbulent flows, nowadays, the most used methods are based on the time-averaged Navier-Stokes equations (RANS), referred to as the Reynolds equations (referrenced in chapter 4 and section 4.2.1).The main specific features of liquid metals are related to the turbulent transport of heat. Regarding the transport of momentum, their behaviour is similar to other Newtonian fluids [12]. However, the transport of momentum has a strong influence in the energy

balance. Therefore, modelling turbulent heat flux is always coupled to a model for the turbulent transport of momentum. For all theoretical considerations regarding turbulent heat transfer, a central problem is given by the evaluation of the turbulent heat flux $\overline{u_i'T'}$. Consequently, it is frequently modelled using the concept of the thermal eddy diffusivity (α_t) and the corresponding turbulent Prandtl number (Pr_t), which we will see with more detail on the following section.

Regarding liquid metal flows, for a steady steate incompressible flow and assuming that the molecular heat flux is governed by the Fourier law of conduction and that there are no source or sinks of mass, momentum and energy, the following energy time-averaged transport equation considering the Reynolds decomposition is obtained [12]:

$$\overline{u_i}\frac{\partial \overline{T}}{\partial x_i} = \frac{\partial}{\partial x_i}\Big(\frac{\nu}{Pr}\frac{\partial \overline{T}}{\partial x_i} - \overline{u_i'T'}\Big) \tag{4.18}$$

and considering:

- Thermal diffusivity for a fluid: $\alpha = \dfrac{\nu}{Pr}$

- For turbulent components: $\alpha_t = \dfrac{\nu_t}{Pr_t}$

$$\sum_j \frac{\partial(\overline{U_jT})}{\partial X_j} = \sum_j \frac{\partial}{\partial X_j}\Big(\alpha\frac{\partial \overline{T}}{\partial X_j} - \overline{u_J'T'}\Big) + \overline{Q} \tag{4.19}$$

We can verify that a new term appears in the energy equation due to time averaging, the turbulent heat flux:

$$q_i'' = \overline{u_i'T'} \tag{4.20}$$

Where α_{eff} is the effective thermal diffusivity.

The following equation for the temperature is implemented:

$$\bigtriangledown \cdot (\overrightarrow{U}\,T) = \bigtriangledown \cdot (\alpha_{eff} \bigtriangledown T) + Q \tag{4.21}$$

Likewise modelling the extra terms that appear in the Navier-Stokes equations due to time averaging, the turbulent heat flow needs to be modelled as well for the closure of the problem. For this purpose, the Reynolds Analogy is used.

4.3   Standard $\kappa - \varepsilon$ model

This model is a general description of turbulence that allows for the effects of transport of turbulence properties by convection and diffusion and for production and destruction of turbulence. RANS turbulence models are classified according to the number of additional transport equations that need to be solved along with the RANS flow equations, and in the case of this model, two transport equations (PDEs) are solved: one for the turbulent kinetic energy κ and a further one for the rate of dissipation of turbulent kinetic energy ε. It is assumed that the turbulent viscosity μ is isotropic. There is also a kinematic turbulent or viscosity ν given by: $\nu_t = \mu_t/\rho$ in m^2/s. The mechanisms that affect the turbulent kinetic energy are the main focus in this model. Eddy viscosity or (turbulent viscosity) is given as follows in Pa.s:

$$\mu_t = \rho C_\mu \frac{\kappa^2}{\varepsilon} \tag{4.22}$$

Where C_μ is a dimensionless constant. The standard $\kappa - \varepsilon$ model uses the following transport equations for κ and ε:

$$\frac{\partial(\rho\kappa)}{\partial t} + \mathrm{div}(\rho\,\kappa\,U) = \mathrm{div}\left[\frac{\mu_t}{\sigma_t}\mathrm{grad}\,\kappa\right] + 2\mu_t S_{ij} \cdot S_{ij} - \rho\,\varepsilon \tag{4.23}$$

$$\frac{\partial(\rho\varepsilon)}{\partial t} + \mathrm{div}(\rho\,\varepsilon\,U) = \mathrm{div}\left[\frac{\mu_t}{\sigma_t}\mathrm{grad}\,\varepsilon\right] + C_{1e}\frac{\varepsilon}{\kappa}2\mu_t S_{ij} \cdot S_{ij} - C_{2\varepsilon}\rho\frac{\varepsilon^2}{\kappa} \tag{4.24}$$

Where:

- First term: rate of change of κ or ε

- Second term: Transport of κ or ε by convection

- Third term: Transport of κ or ε by diffusion

- Fourth term: Rate of production of κ or ε

- Fith term: Rate of destruction of κ or ε

These equations contain the following adjustable constants: $C_\mu, \sigma_\kappa, \sigma_\varepsilon, C_{1\varepsilon}C_{2\varepsilon}$, which assume these values for a wide range of turbulent flows:

$$C_\mu = 0.009 \qquad \sigma_\kappa = 1.00 \qquad \sigma_\varepsilon = 1.30 \qquad C_{1\varepsilon} = 1.44 \qquad C_{2\varepsilon} = 1.92 \tag{4.25}$$

σ_κ and σ_ε are the Prandtl numbers connecting the diffusivities of κ and ε to the eddy viscosity μ_t. The factor ε/κ in the rate of production and destruction terms 4.24 makes these terms dimensionally correct in the ε equation. Constants $C_{1\varepsilon}$ and $C_{2\varepsilon}$ provide the correct proportionality between the terms in the $\kappa - \varepsilon$ equations.

The following boundary conditions are necessary due to the elliptic nature of the model equations for κ and ε as result of the gradient diffusion term:

- Inlet: distribution of κ and ε must be given

- Outlet/symmetry axis: $\dfrac{\partial\kappa}{\partial n} = 0$ and $\dfrac{\partial\varepsilon}{\partial n} = 0$ (zero gradient)

- Free stream: κ and ε must be given or $\dfrac{\partial\kappa}{\partial n} = 0$ and $\dfrac{\partial\varepsilon}{\partial n} = 0$ (zero gradient)

- Solid walls: approach depends on Reynolds number.

Regarding the boundary conditions for solid walls, at high Reynolds number, the standard $\kappa - \varepsilon$ model (Launder and Spalding, 1974) takes advantage of the universal behaviour of near-wall flows. The turbulent kinetic energy at the inlet κ_i, is given by:

$$\kappa_{in} = \frac{1}{2}(u_x'^{\,2} + u_y'^{\,2} + u_z'^{\,2}) \tag{4.26}$$

Turbulence intensity is given as follows:

$$I_U = \frac{\frac{2}{3}k^{1/2}}{U_{ref}} \tag{4.27}$$

The mass flow rate at the outlet of the pumps, as stated before, is of 9440.44 kg/s. Therefore the turbulent kinetic energy κ at the inlet is calculated as:

$$\kappa_{in} = \frac{1}{2}(u_x'^2 + u_y'^2 + u_z'^2) = \frac{1}{2}\left[u_x'^2 + 2\left(\frac{1}{3}u_x'\right)^2\right] = \frac{11}{18}(I_U \cdot U_x)^2 \tag{4.28}$$

According to Jischa (1982), common turbulence are 1% downstream of a sieve, 10% close to a wall and above 10% in a free jet. In conclusion, considering a turbulence intensity level I_U of 10% and a velocity of 2.45 m/s extracted form a preliminary calculation, this return: $\kappa_{in} = 0.15$ m$^2 \cdot$ s^{-2} Turbulent dissipation ε is given by:

$$\varepsilon_{in} = \frac{C_\mu^{0.75}\ k_{in}^{1.5}}{l} \tag{4.29}$$

where $C_\mu = 0.09$ and the turbulent length scale l is approximated as 7% of the hydraulic diameter D_H, therefore: $\varepsilon_{in} = 1.3637$ m$^2 \cdot$ s^{-3}. Lastly, an outlet pressure of 0 Pa , equal to the operating pressure, is applied to the pump's inlet. Considering the following conditions and the eddy viscosity formula 4.22:

- y the coordinate direction normal to a solid wall.

- y_p a point with $30 < y_p{}^+ < 500$.

- the mean velocity at y_p satisfies the log-law: $u^+ = y^+$.

- the measurements of turbulent kinetic energy budgets indicate that the rate of turbulence production is the same as the rate of dissipation.

We can obtain the following wall functions, relating the local wall shear stress (u_τ) to the mean velocity, turbulence kinetic energy and rate of dissipation:

$$u^+ = \frac{U}{u_\tau} = \frac{1}{\Bbbk}ln(Ey_p{}^+) \tag{4.30}$$

where:

- $\Bbbk = 0.41$ - von Karman's constant

- $E = 0.98$ - wall roughness parameter for smooth walls

4.3.1 Thermal modelling - Reynolds analogy

The Reynolds analogy relates momentum transfer and heat transfer and considers a constant Pr_t number (turbulent Prandtl number). Once the mesh was generated after 5.1, the Reynolds Analogy was implemented considering a Prandtl turbulent number of 2.0.

As stated in 5.2.1, the used solver was the *myrrhaSimpleFoam*, developed at the von Karman Institute.

According to Reynolds analogy, it is assumed that the value of the turbulent or eddy diffusivity Γ_t is fairly close to that of turbulent viscosity μ_t, as turbulent transport of momentum and heat or mass is due to eddy mixing. A turbulent Prandtl/Schmidt number is defined:

$$\sigma_t = \frac{\mu_t}{\Gamma_t} \tag{4.31}$$

Regarding this analogy, it is assumed that this ratio value is around unity, since many experiments have established that this ratio is often nearly constant. Nonetheless, this is not the case with

regards to heavy liquid metals. In liquid metal flows, the Pr_t is larger than the unit given their large molecular thermal conductivity compared to its molecular viscosity.

The turbulent Prandtl number differs from the molecular Prandtl number since it quantifies the ratio between the momentum and the thermal diffusivity at the eddy scale. Therefore, energy is more easily transferred to the adjacent fluid compared to momentum. Consequently, the Pr_t increases as the Pr decreases [12]. The choice of the turbulent Prandtl number lies on recent studies, which suggest an average Pr_t between 1 and 4 with a peak at the wall and a decreasing value with wall distance, stabilizing at around 1. Hence, an accurate solution should lie for $1 < Pr_t < 2.8$, according to the previous performed study Democritos [4].

4.4 Boundary Conditions

Computational schemes and specifications of boundary conditions depend on the types of PDE's implemented in the CFD model. Often, the governing equations in fluids and heat transfer are of mixed types and therefore the selection of computational schemes and methods to apply boundary conditions is a matter of great importance in CFD. [21]. In the tables presented in the Appendix, the boundary conditions are detailed. It should be noted that the free surfaces were modelled with the *slip* boundary condition. To summarize [22]:

- calculated - This boundary condition is not designed to be evaluated; it is assmued that the value is assigned via field assignment.

- fixedValue - This boundary condition supplies a fixed value constraint, and is the base class for a number of other boundary conditions.

- zeroGradient - This boundary condition applies a zero-gradient condition from the patch internal field onto the patch faces.

- fixedFluxPressure - This boundary condition sets the pressure gradient to the provided value such that the flux on the boundary is that specified by the velocity boundary condition.

- slip - This boundary condition provides a slip constraint.

- flowRateInletVelocity - This boundary condition provides a velocity boundary condition, derived from the flux (volumetric or mass-based), whose direction is assumed to be normal to the patch.

- nutkWallFunction - This boundary condition provides a turbulent kinematic viscosity condition when using wall functions, based on turbulence kinetic energy.

- epsilonWallFunction - This boundary condition provides a turbulence dissipation wall function condition for high Reynolds number, turbulent flow cases. The condition can be applied to wall boundaries, whereby it calculates ε and G inserts near wall epsilon values directly into the epsilon equation to act as a constraint.

- kqRWallFunction - This boundary condition provides a suitable condition for turbulence fields for the case of high Reynolds number flow using wall functions.

- alphatJayatillekeWallFunction - This boundary condition provides a kinematic turbulent thermal conductivity for using wall functions, using the Jayatilleke 'P' function.

- groovyBC - A boundary condition that allows arbitrary expressions in the field-file. This boundary condition is basically a mixed-BC where value, gradient and valueFraction are specified as expressions instead as fields. [23]

For the inlet, the volumetric flow rate is of 0.4545 m³/s. $\left(Q = \dfrac{\dot{m}}{\rho} = \dfrac{9440.4/2}{10377.1} \right)$
As stated in 4.3, the values of κ and ε are of 0.15 and 1.3637 respectively. The choice of the boundary conditions is also explained in that section.

4.5   Numerical Schemes

In this section, an approach of the numerical schemes for terms calculated during the simulation is made. These terms are for example derivatives (gradients) and interpolation of values from a group of points to another. The discretisation used in this study case is the Gaussian finite volume integration. This consists on summing values on cell faces, which must be interpolated from cell centres [24].

4.5.1   Time schemes

As the study case considers a steady flow, the time scheme used is *steadyState* which sets time derivatives to zero.

4.5.2   Gradient schemes

The discretisation scheme used for the gradient terms is the *Gauss linear* The Gauss entry specifies the standard finite volume discretisation of Gaussian integration which requires the interpolation of values from cell centres to face centres. The interpolation scheme is then given by the linear entry, meaning linear interpolation or central differencing. In the case of the myrrhaSimpleFoam solver, for the gradient of pressure at the cells interface, the variables are first interpolated to the faces before calculating the gradient [4].

4.5.3   Divergence schemes

The divergence terms are discretised with resource to *bounded Gauss upwind* and *Gauss linear*. For the non-advective terms, the Gauss integration with linear interpolation is used. As for the advective terms, the bounded Gauss upwind is used. The upwind schemes distinguishes between upstream and downstream influences (wave propagation directions).

4.5.4   Surface normal gradient scheme

A surface normal gradient is evaluated at a cell face; it is the component, normal to the face, of the gradient of values at the centres of the 2 cells that the face connects. The chosen scheme is the *uncorrected*, as it applies under-relaxation without non-orthogonal correction

4.5.5   Laplacian schemes

Here, the Laplacian terms (the diffusion term in the momemntum equations) are discretised according to the *Gauss linear corrected scheme*. The diffusion coefficient is interpolated according to the Gauss linear interpolation. Since the mesh is non-orthogonal, in order to maintain

second-order accuracy, an explicit non-orthogonal correction is added to the orthogonal component, therefore the corrected scheme for the surface normal gradient scheme.

4.6   Solution and algorithms

The solver is the method used to solve a matrix equation, for each discretised equation. For the present study, the linear-solvers used were PBiCG (for asymetric matrices, introduced by advective derivatives which is a derivative taken with respect to a moving coordinate system) and GAMG (generalised geometric-algebraic multi-grid). The latter uses Gauss-Seidel as a smoother.

4.6.1   Algorithm

Between the three possible algorithms to be used (PISO, PIMPLE and SIMPLE), the selected one was the SIMPLE (Semi-implicit method for pressure-linked equations) algorithm given the steady-state nature of the flow. The algorithm is an iterative process for coupling equations for momentum and mass conservation.

4.6.2   Under relaxation factors

Under-relaxation is a technique used to improve stability of a computation, more specifically in steady-state problems. The process consists in limiting the amount that a variable changes from one iteration to the next, either by modifying the solution matrix and source prior to solving for a field or by modifying the field itself. The amount of under-relaxation is specified by the under-relaxation factor α, that takes values between 0 and 1 [24]. It is crucial to select the correct under-relaxation factors (α) in order to obtain cost-effective simulations. If the value of α is too big, the iterative solutions might be oscillatory or even diverge. On the other hand, exceedingly slow divergence might be caused by the choice of a very small value of α. In the present work, under-relaxation factors were used to achieve convergence of the solution, as shown in table A.1 in the Appendix A.

Chapter 5

Single-phase mesh without conjugated heat-transfer

Chapter 2 contains a CFD overview, where pre-processing, solver and post-processing are explained. In the present chapter, the implementation of these steps to the model in study, in nominal conditions, are presented.

5.1 Pre-processing

5.1.1 *snappyHexMesh* - pre-processing

"snappyHexMesh" is an utility of OpenFOAM used to generate a mesh, therefore it is a pre-processing tool. It generates a 3D mesh consisting of hexahedra (hex) and split-hexahedra (split-hex) automatically from triangulated surface geometries, or tri-surfaces, in Stereolithography (STL) or Wavefront Object (OBJ) format, through three different steps (castellatedMesh, snapping and addLayers). Over an iterative process, the primary mesh is refined while conforming to the surface and morphing the resulting split-hex mesh to the surface. Then, the refined mesh is snapped to the surfaces to capture the geometric complexity correctly. Optionally, it is possible to shrink back the resulting mesh and insert cell layers (final step). The user has freedom to decide the level of refinement of the mesh. The mesh quality controls define the final quality parameters of the mesh. This utility runs in parallel with a load-balancing step every each iteration.

snappyHexMesh was the chosen utility as it is automatic and able to run in parallel, making it easier and faster to reach the solution given the complex and heavy mesh of the study case. The mesh was refined 3 times around the edges of the geometry in study and 4 times around the surfaces and no boundary layer was inserted. Besides, 3 different regions were defined in order to capture both pump jets (2 cylinders) and the jet below the core (1 cylinder).

A grid dependence study was performed, by successively refining the initial coarse grid of the basic mesh, until the best mesh was obtained. Finally, a final mesh was obtained by following the steps stated in the following paragraph.

Firstly, an initial block (containing the geometry) is generated with the file *blockMeshDict*. The dimensions of this block are: (65 x 65 x 85) m, totalizing 363350 cells. Secondly, the set up in *snappyHexMesh* is made in order to generate the mesh, with defined refined regions below the core and the pumps and near the walls. A refined mesh is obtained, as seen in the figure 5.1.

The three refinement regions, referenced previously, can be denoted in the mesh around both pump jets and the jet below the core.

The statistics of the mesh are summarized in table 5.1 while the overall number of cells is summarized in table 5.2.
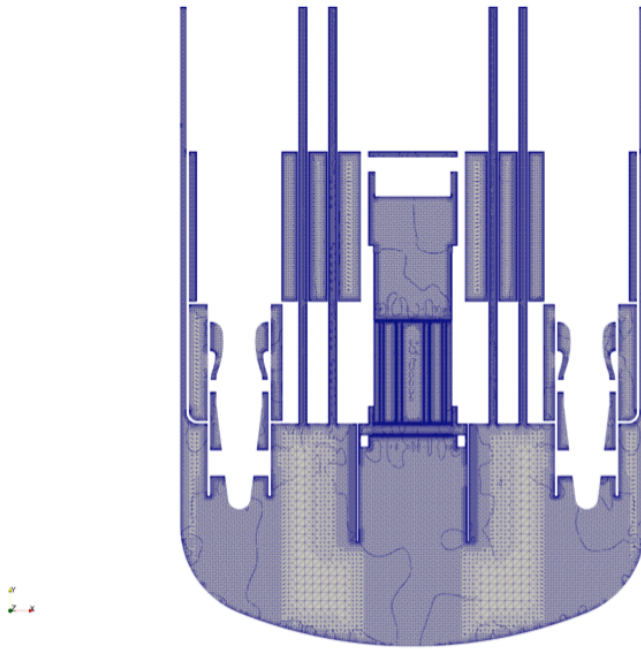
Figure 5.1: Generated mesh

Table 5.1: Mesh statistics

Points	27462012
Faces	93295332
Internal faces	84042576
Cells	28049384
Faces per cell	6.322346
Boundary patches	55
Point zones	0
Face zones	13
Cell zones	13

Table 5.2: Overall number of cells of each type

Points	27462012
Hexahedra	21253332
Prisms	2539868
Wedges	0
Pyramids	0
Tet wedges	11632
Tetrahedra	0
Polyhedral	4244552

5.2   Solver

5.2.1   myrrhaSimpleFoam

As stated before, the solver used for this study is the *myrrhaSimpleFoam*. This solver was developed in order to respond to the need of simulating buoyant flow and transient flow with a porous media approach, all simultaneously.

Once the mesh was obtained, the solver *myrrhaSimpleFoam* was used with the goal of analysing the heat transfer effect in the reactor. Complemented with the most relevant thermal turbulence models for low Prandtl numbers currently, this tool deals with incompressible buoyancy corrected steady/unsteady single-phase flows. It solves the Reynolds-Averaged Navier-Stokes equations (RANS) (4.2.1) with temperature as scalar in the single-phase environment. Pressure and velocity field are coupled using the SIMPLE algorithm. The momentum and turbulence models are extended to buoyant flows. The RAS turbulence model $\kappa - \varepsilon$ is used and in order to predict the effect of turbulence heat transfer, the Reynolds analogy is implemented, with a constant turbulent Prandtl number of 2.0.

5.3   Post-processing

In this section, the results of the simulation and the correspondent post-processing performed are presented. The steady-state simulation ran in with 40 processors and with 1500 iterations with a size of 7.231GB and finalizing after a CPU time of 1:18:44:09 and a Wallclock Time (real time) of 10h49m.

5.3.1   Velocity field

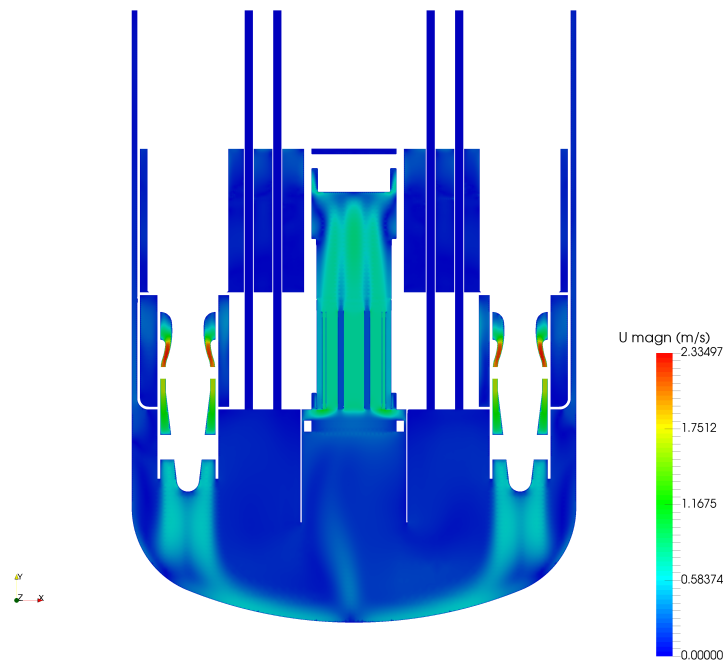The following image 5.2 shows the velocity field obtained:

Figure 5.2: Velocity field

5.3.1.1   Flow field

As observed in figure 5.4 firstly the two pump jets impact the bottom of the vessel before cooling in the centre of the reactor, leading to a characteristic layer of ascendant flow towards

the core.

In the core, the flow is distributed through the different core rings, after which the several jets tend to merge in the plane of the two pumps. However, it does not reach the free surface due to the plug.

Lastly, the flow in the upper plenum goes back into the heat exchanger. It is possible to see that all the flow that enters the heat exchanger, exits though its outlets. The nominal mass flow rate originates a maximum velocity of 2.346 m/s in the pumps, originated by the nominal mass flow rate.

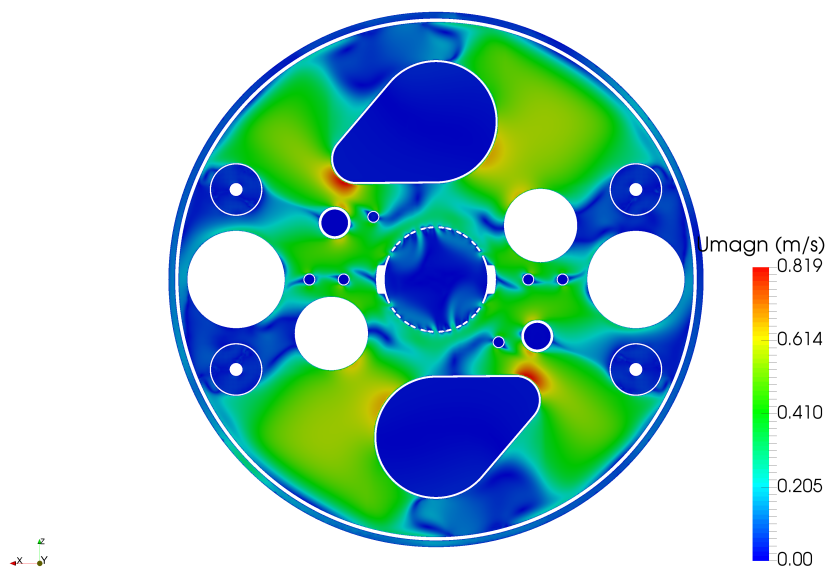Finally, in 5.3 we can see the velocity contours on the LBE surface.

Figure 5.3: Velocity magnitude on the free-surfaces

5.3.2 Pressure

The overall pressure drop through the primary coolant loop obtained is of approximately 2.37 bar, as seen in figure 5.5.

As stated before in chapter 3, porous media section 3.6.1, one of the most important parameters of the reactor is the pressure drop through the core. As expected, the pressure drop is of 1.7 bar. On the other hand, the pressure drop between the cold plenum and the hot plenum is of around 1.86 bar, while the expected one is of 2 bar. In the graphic in 5.6 it is possible to observe the axial pressured drop along the core obtained with OpenFOAM:

In the 5.7, the pressure contours on the LBE free-surfaces are presented.

Here, it can be seen a difference of 1.78 bar between the free-surfaces of the main walls and the hot plenum plate.
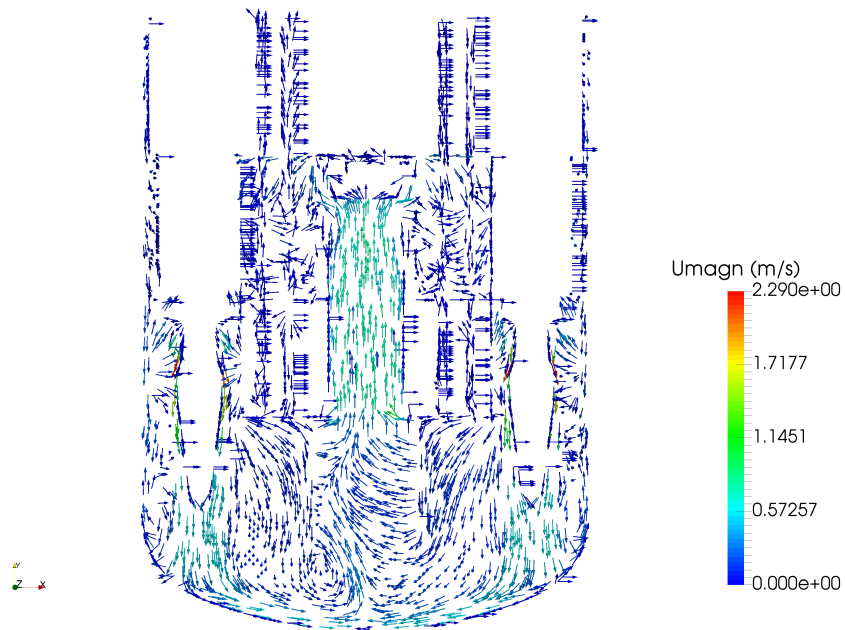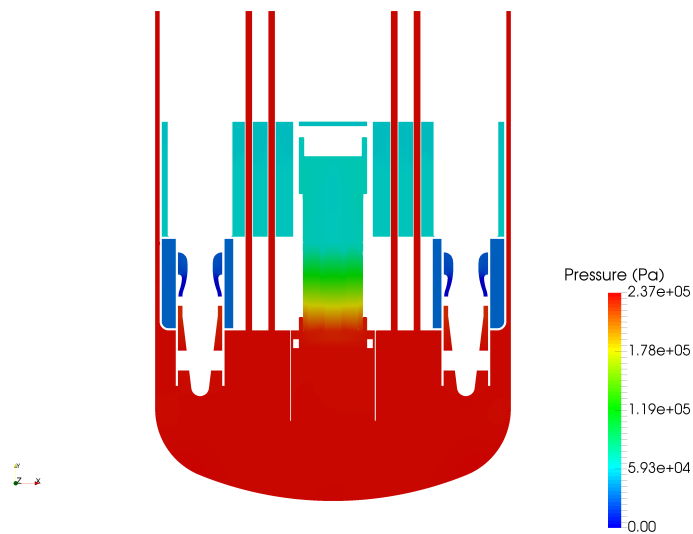
Figure 5.4: Velocity field - vector

Figure 5.5: Static pressure

5.3.3   Temperature

Firstly, it should be taken in account that the results are for a turbulent Prandtl number of 2.0. It can be verified in 5.8 that the temperature does not exceed 757 K. This is according to the conditions imposed.

In 5.10 the temperature field in the core and the graphic of this variation is shown. The temperature difference in this area is of around 237 K.

Temperature variations are verified all over the reactor due to several heat sources and sinks
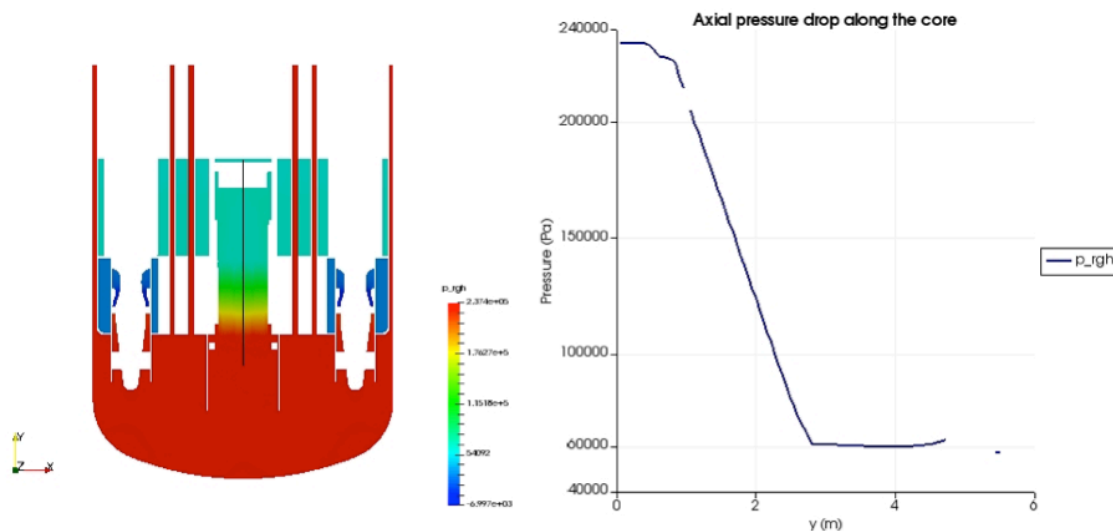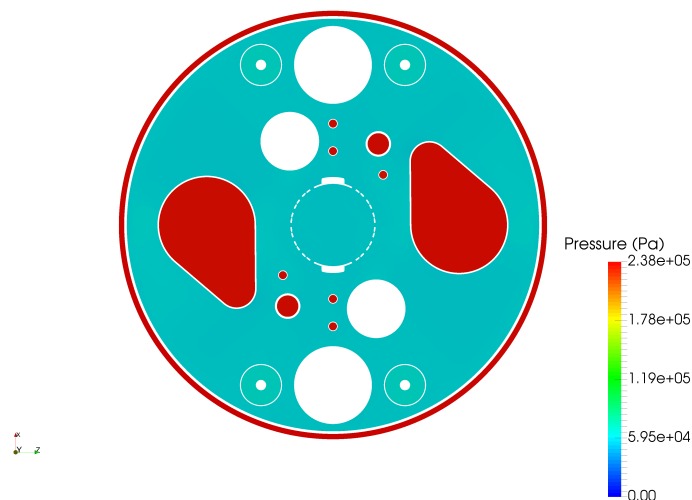
Figure 5.6: Pressure drop in the core (x,z=0)

Figure 5.7: Pressure in the LBE free surfaces

implemented for thermal modelling. A power of 100 MW is injected across the core and an additional 2 MW are added in total in the IVFS, as mentioned previously, where the used FA are stored. This same amount of heat (102 MW) is extracted by the four HX since thermal losses to the exterior are neglected for the moment. The turbulent Prandtl number was fixed to 2.0.

The core heat source located in the inner and outer FA rings heats up the flow coming out from the other rings as the flow rises, caused by mixing. A maximum temperature of 757 K is reached in the core. The mass flow average core inlet and outlet temperatures correspond to an average of 540 K and 620 K respectively, in agreement with an injected power of 100 MW ($P = \dot{m}C_p\Delta T$).
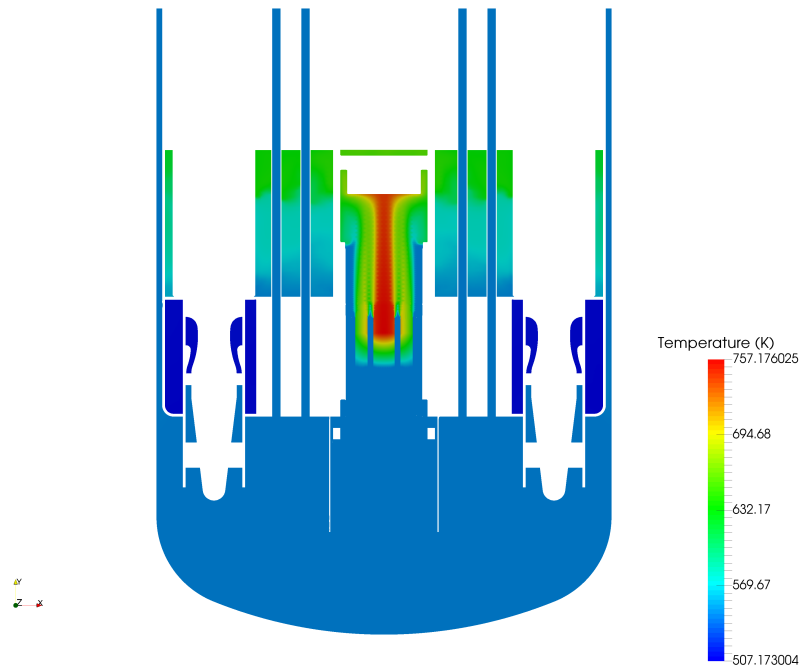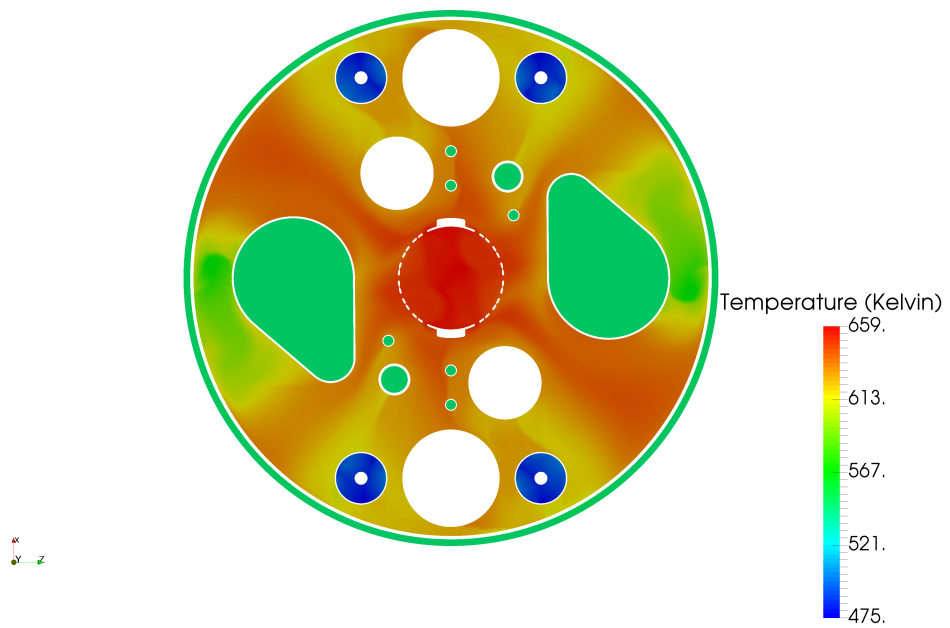
Figure 5.8: Temperature countours

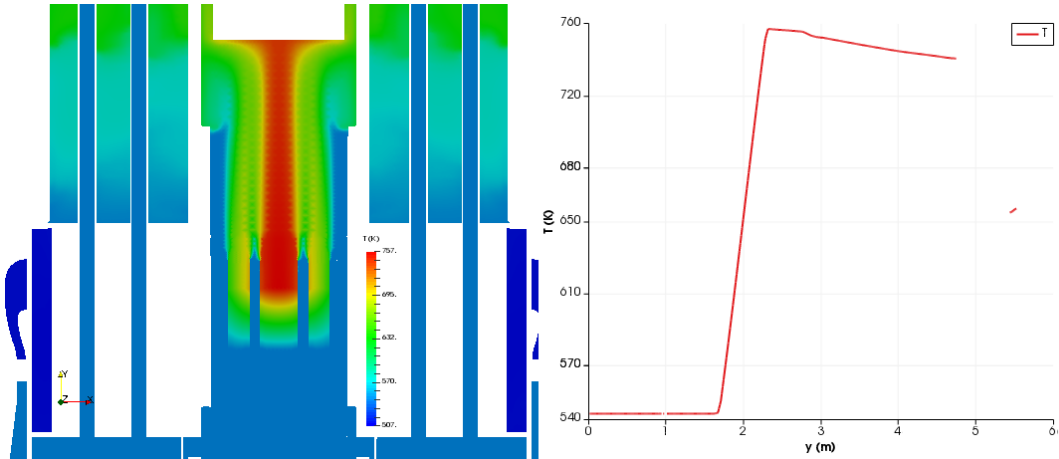
Figure 5.9: Temperature countours in the free surfaces

Figure 5.10: Temperature variation throughout the core

Chapter 6

Conclusions and future work

6.1 Results - Comparison with Democritos

In this section a comparison is made between the results of the present study and part of the study "CFD – Migration of steam and dispersion of solid elements" [4], involved in the Democritos project. It is important to state that this is a confidential document. The Democritos document covered four main topics:

1. Selection of a flexible mesh generator to enable fast re-meshing of the geometry in case of version changes

2. Numerical modelling of the reactor in nominal conditions including all the necessary physics in both ANSYS-Fluent and OpenFOAM for comparison purposes

3. Verification of the developed myrrhaFoam OF solver by confrontation to the ANSYS-Fluent simulation of the full reactor and thermal-hydraulic description of the reactor in nominal conditions

4. Analysis of CHT effects in ANSYS-Fluent and implementation in the solver

Consequently, this dissertation and the Democritos study have in common the numerical modelling in the OpenFOAM environment in nominal conditions, and the implementation of the *myrrhaSimpleFoam* solver, referred as *myrrhaFoam* in the Democritos project.

In the present study, the confrontation with software ANSYS-Fluent and analysis of CHT effects were not developed.

6.1.1 Geometry

First of all, some considerations regarding geometry discrepancies need to be taken into account. While in the present study the considered design is v1.6, in Democritos v1.4 is used.

In the Democritos study, the original barrel has 11 rows of ten 200 mm holes at is periphery. Nonetheless, in order to match the numerical domain where the LBE is present, delimited by the free-surface level, the CAD file was adjusted. The surface level was positioned in the middle of the 7th row (from the bottom) of barrel holes. In conclusion, the upper part of the barrel was ommited from the geometry. In version 1.6, the full barrel is considered.

The ACS has two grids located at intermediate positions. This can be verified in figure 6.1.

6.1.2 Pressure

While in the Democritos document the overall pressure drop obtained is of around 2.57 bar (see 6.2), in the present work an overall pressure drop of 2.37 bar was obtained, as stated in section 5.1.
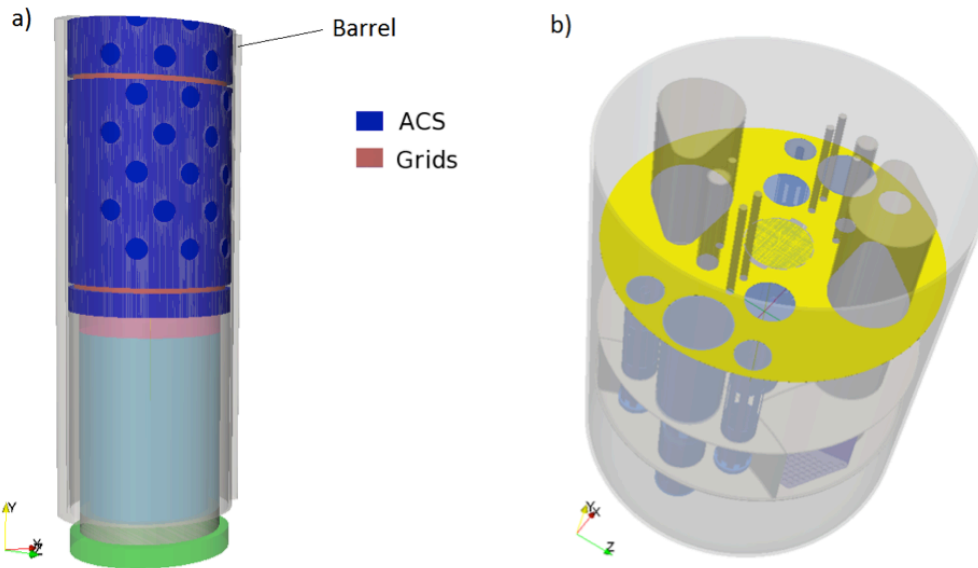
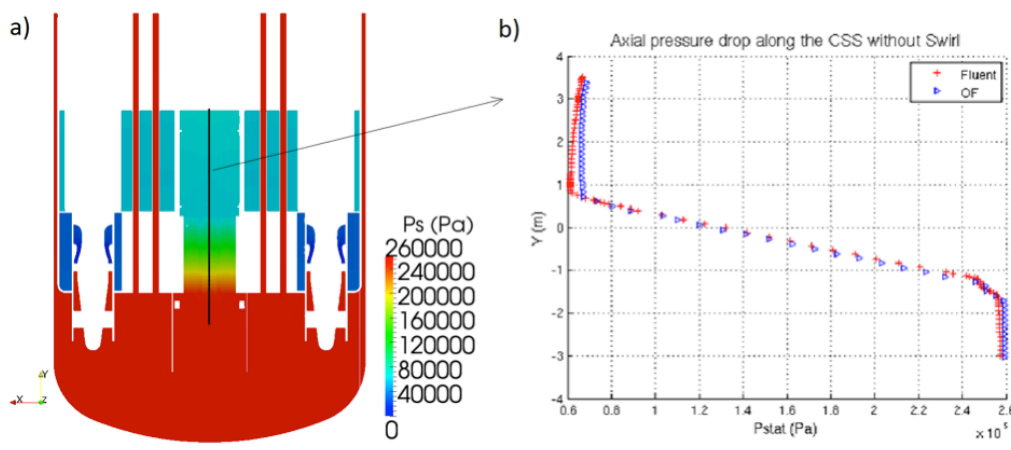Figure 6.1: Democritos: a) Porous media representation of the ACS b) Hot plenum and barrel free-surfaces

Figure 6.2: Democritos: a) Static pressure contours in the vertical symmetry plane x = 0 m [ANSYS Fluent] b) Comparison of static pressure evolution along the core central line x,z=0m.

Since the two free-surfaces are positioned in the middle of the 7th row of barrel holes in the version 1.4, while in the present work the barrel is around 20 cm higher, differences are observed in the flow. With reference to figure 6.3, a difference in pressure between the barrel and the HP free-surfaces of about 6 kPa is obtained, corresponding to a difference in height of 6 cm. In figure 5.7 the pressure difference between the HP and the barrel is inexistent since there are more holes and all the flow exits through this holes. Consequently, the pressure is the same inside and outside the barrel. The latest design is proven to be more adequate.

6.1.3 Velocity

It is possible to verify that the velocity fields are slightly different in both studies. In the present study, the velocity in the primary circuit is stabilized, therefore before entering the core the velocity is lower compared to the one in version 1.4.
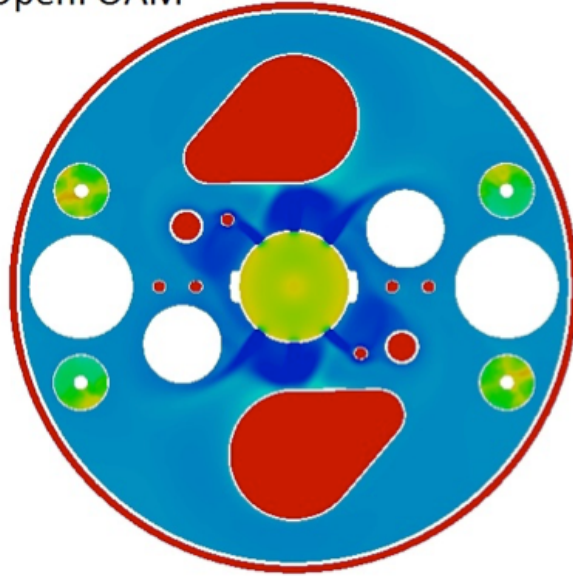
44

Figure 6.3: Democritos: Static pressure contours on the LBE free-surface
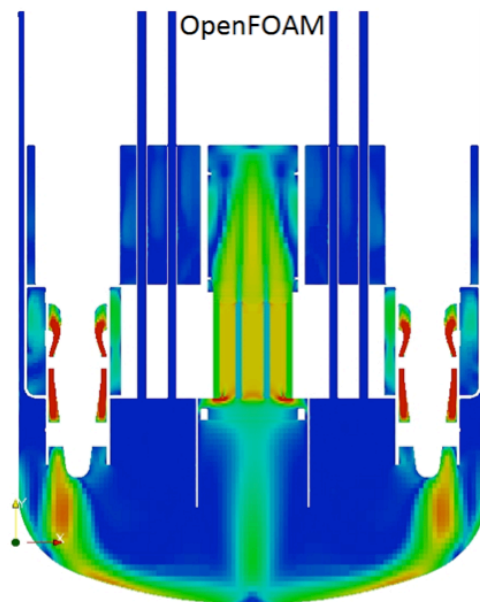
Figure 6.4: Democritos: Velocity magnitude contours in the vertical symmetry plane z=0

The maximum velocity achieved in the pumps is the approximately the same in both versions of the design, being around 2.37 m/s in version 1.4 and 2.346 m/s in v1.6.

6.1.4 Temperature

The maximum temperature in the core in version 1.4 was around 741 K, while in the present study was of approximately 757 K which is not a very considerable difference. However, these values are higher than the allowable maxium one: 466 ℃ ($\approx$ 739.15 K).

In the Democritos study, the considered turbulent Prandtl number is of 2.8. Regarding this parameter, differences can be noticed in the hot plume of the core. It is notable that the temperature diffusion is higher when considering the results with a $Pr_t = 2.0$. This was also
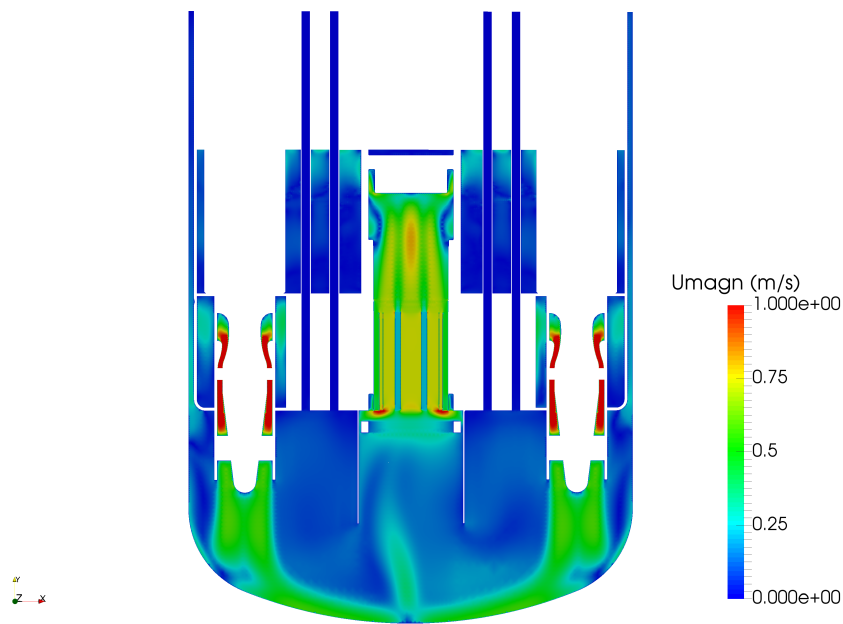
Figure 6.5: Velocity field in version 1.6

verified in previous performed studies: with increasing temperature diffusion the Pr_t decreases (with reference to figure 6.6).
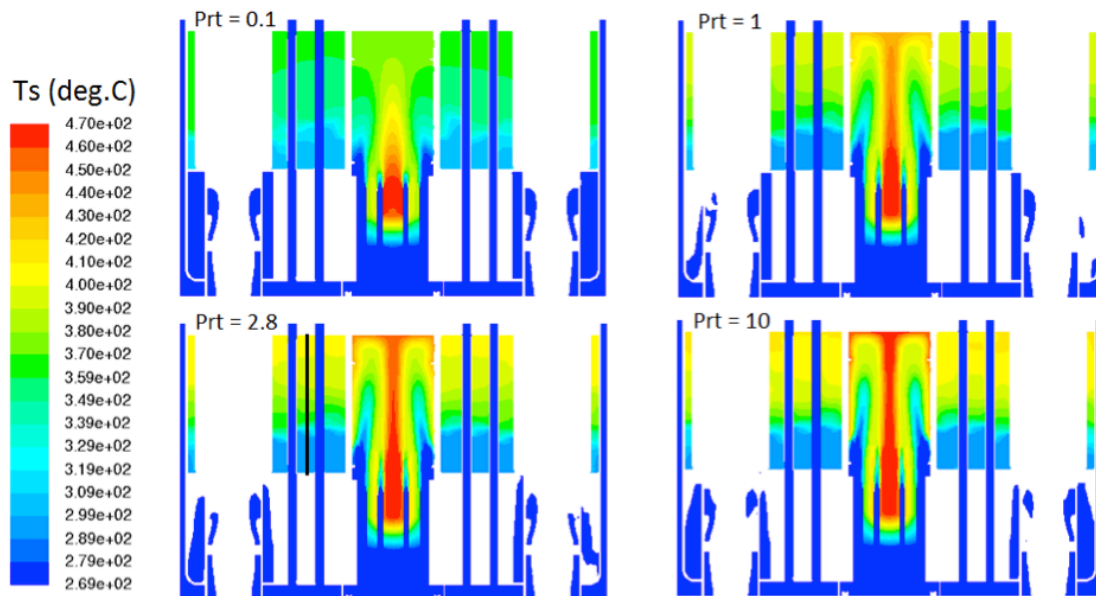
Figure 6.6: Democritos: Effect of Pr_t on static temperature contours in the plane (z=0)

In version 1.4, high temperatures rise along the outer vessel wall, which does not happen in version 1.6. This is because the simulation performed for this dissertation ran with less iterations, not reaching a point where the temperature increased as much. Nonetheless, this happens in v1.4 because very high temperatures are reached in the IVFS due to the low velocity values in this zone, causin gthe hot flow to exit through the inner vessel holes and to rise along the

outer vessel wall. This can be corrected with a conjugated heat transfer study, by improving the boundary conditions and by considering conduction through the solid walls.

6.1.5 Limitations

Over the course of 4 months, numerous simulations were performed, which the majority was not concluded due to various obstacles and problems given the complex geometry of the reactor and consequent difficulty to obtain a model that would run until the end.

A second mesh (less refined) was obtained by modifying the blockMesh file, this time with the following dimensions: (54 x 54 x 72) m, totalizing 209952 cells. After running *snappyHexMesh* with 8 processors, a mesh with 57291341 cells was obtained.

The *myrrhaSimpleFoam* was also implemented in this mesh, however it diverged and due to lack of time given the heavy mesh and the necessary time to run, it was not possible to achieve a converged solution. Further modifications of the set-up would have to be made.

Besides, it was also proposed to perform a study case with conjugated heat transfer (CHT), however this was not possible due to lack of time.

6.2 Conclusions

This study presents a numerical simulation of the MYRRHA reactor design version 1.6, being its CFD model performed by the author. The purpose of this study was to analyze the overall flow field in the reactor, as well as to perform its thermal modelling. As expected, it was a challenging study due to the complex nature of the geometry.

In the reactor, the flow exits the pumps in the form of jets and impacts the bottom of the vessel. Then, after bein cooled, it rises to the core and enters it. Then, it is distributed through the core rings but does not reach the free surface due to the existence of the plug. Finally, the flow goes back into the PHX and exits though its outlet.

The maximum reached temperature is of 757 K, which is a value above the allowable temperature in nominal conditions. This can be corrected by implementing conjugate heat transfer.

The pressure drop were also as expected between the free surface and the hot plenum, being around 1.78 bar. Throughout the core, the pressure drop was of 1.7 bar.

It is possible to conclude that the design version 1.6 is indeed an improvement in relation to version 1.4.

6.3 Future work

This project has several scenarios to study and investigate. In the future, it might be suggested to continue this study while:

- implementing conjugated heat transfer (CHT). This considers the heat transfer and exchange of energy between solid and fluid domains. A multiregion mesh is required to define clearly the different interfaces in the computational model.

- improving the boundary conditions, this way it is possible to obtain better values and more accurate results.

- analysing the high temperature gradients that result from the conjugated heat transfer.

Experimental work can also be complementary to this study, by comparing the numerical and experimental results.

Bibliography

[1] N. Chapman and C. McCombie, Principles and standards for the disposal of long-lived radioactive wastes.   Elsevier, 2003, vol. 3. 1

[2] H. Takano, K. Nishihara, K. Tsujimoto, T. Sasa, H. Oigawa, and T. Takizuka, "Transmutation of long-lived radioactive waste based on double-strata concept," Progress in Nuclear Energy, vol. 37, no. 1-4, pp. 371–376, 2000. 1

[3] M. Salvatores, I. Slessarev, G. Ritter, P. Fougeras, A. Tchistiakov, G. Youinou, and A. Zaetta, "Long-lived radioactive waste transmutation and the role of accelerator driven (hybrid) systems," Nuclear Instruments and Methods in Physics Research Section A: Accelerators, Spectrometers, Detectors and Associated Equipment, vol. 414, no. 1, pp. 5–20, 1998. 1

[4] L. Koloszar, S. Buckingham, P. Rambaud, and P. Planquart, "Cfd – migration of steam and dispersion of solid elements - final report democritos phase 2 [confidential]," von Karman Institute for Fluid Dynamics, Tech. Rep., 2012/2013. 2, 9, 31, 32, 43

[5] H. K. Versteeg and W. Malalasekera, An introduction to computational fluid dynamics: the finite volume method.   Pearson Education, 2007. 3, 5, 6, 27

[6] R. H. Pletcher, J. C. Tannehill, and D. Anderson, Computational fluid mechanics and heat transfer.   CRC Press, 2012. 3

[7] C. Greenshields, "CFD Direct," https://cfd.direct/openfoam/about, [Online]. 6

[8] F. Moukalled, L. Mangani, M. Darwish et al., The finite volume method in computational fluid dynamics.   Springer, 2016. 6

[9] J. Blazek, Computational fluid dynamics: principles and applications.   Butterworth-Heinemann, 2015. 6

[10] J. Tu, G. H. Yeoh, and C. Liu, Computational fluid dynamics: a practical approach.   Butterworth-Heinemann, 2012. 6

[11] H. A. Abderrahim, P. Baeten, B. Neerdael, D. Naidoo, D. De Bryuyn, R. Fernandez, G. Van den Eynde, D. Vandeplassche, G. Scheveneels, M. A. N. Ottolini, R. O. T. Shuff, and S. Michiels, "Myrrha technical description [confidential]," von Karman Institute for Fluid Dynamics, Tech. Rep., October 2011. 7

[12] C. Fazio, V. Sobolev, A. Aerts, S. Gavrilov, K. Lambrinou, P. Schuurmans, A. Gessi, P. Agostini, A. Ciampichetti, L. Martinelli et al., "Handbook on lead-bismuth eutectic alloy and lead properties, materials compatibility, thermal-hydraulics and technologies-2015 edition," Organisation for Economic Co-Operation and Development, Tech. Rep., 2015. 8, 23, 27, 28, 31

[13] W. Sobieski and A. Trykozko, "Darcy's and forchheimer's laws in practice." Technical Sciences/University of Warmia and Mazury in Olsztyn, 2014. 9, 11

[14] R. Nowak, "Estimation of viscous and inertial resistance coefficients for various heat sink configurations," Procedia Engineering, vol. 157, pp. 122–130, 2016. 11

[15] N. E. Todreas and M. S. Kazimi, Nuclear systems: thermal hydraulic fundamentals.   CRC press, 2012, vol. 1. 17

[16] W. Pfrang and D. Struwe, Assessment of correlations for heat transfer to the coolant for heavy liquid metal cooled core designs.   FZKA, 2007, vol. 7352. 19

[17] K. Mikityuk, "Heat transfer to liquid metal: review of data and correlations for tube bundles," Nuclear Engineering and Design, vol. 239, no. 4, pp. 680–687, 2009. 19

[18] T. Abram and S. Ion, "Generation-iv nuclear power: A review of the state of the science," Energy Policy, vol. 36, no. 12, pp. 4323–4330, 2008. 22

[19] Y. Nakayama, Introduction to fluid mechanics.   Butterworth-Heinemann, 1998. 25

[20] MIT, "Basics of Turbulent Flow," http://www.mit.edu/course/1/1.061/www/dream/SEVEN/SEVENTHEORY.PDF, [Online]. 25

[21] T. Chung, Computational fluid dynamics.   Cambridge university press, 2010. 31

[22] Openfoam.com, "A.4 Standard boundary conditions," http://www.openfoam.com/documentation/user-guide/standard-boundaryconditions.php, [Online]. 31

[23] B. Gschaider, "Contrib/swak4Foam," https://openfoamwiki.net/index.php/Contrib/swak4Foam, [Online]. 32

[24] C. Greenshields, "User Guide," https://cfd.direct/openfoam/user-guide/, [Online]. 32, 33

Appendix A

Appendix

A.1   Under relaxation factors

Table A.1: Under relaxation factors

Variables	Under relaxation factor α
p_{rgh}	0.1
U	0.5
T	0.2
κ	0.3
ε	0.3
κ_t	0.7
ε_t	0.7

A.2   Boundary Conditions

Table A.2: Velocity (U)

Boundary	Boundary condition
Inlet	flowRateInletVelocity
Outlet	zeroGradient
Walls	fixedValue
Cover inter vessel	slip
Cover cold	slip
Cover barrel	slip
Cover hot	slip

Table A.3: Temperature (T)

Boundary	Boundary condition
Inlet	fixedValue
Outlet	zeroGradient
Walls	zeroGradient
Wall vessel 2	groovy BC
Wall upper	groovy BC
Cover inter vessel	slip
Cover cold	slip
Cover barrel	slip
Cover hot	slip

Table A.4: Pressure (p)

Boundary	Boundary condition
Inlet	fixedFluxPressure
Outlet	fixedValue
Walls	fixedFluxPressure
Cover inter vessel	slip
Cover cold	slip
Cover barrel	slip
Cover hot	slip

Table A.5: Turbulent Viscosity μ_t

Boundary	Boundary condition
Inlet	Calculated
Outlet	Calculated
Walls	nutkWallFunction
Cover inter vessel	slip
Cover cold	slip
Cover barrel	slip
Cover hot	slip

Table A.6: Rate of dissipation turbulent kinetic energy ε

Boundary	Boundary condition
Inlet	fixedValue
Outlet	zeroGradient
Walls	epsilonWallFunction
Cover inter vessel	slip
Cover cold	slip
Cover barrel	slip
Cover hot	slip

Table A.7: Turbulent thermal diffusivity α_t

Boundary	Boundary condition
Inlet	calculated
Outlet	calculated
Walls	alphatJayatillekeWallFunction
Cover inter vessel	slip
Cover cold	slip
Cover barrel	slip
Cover hot	slip

Table A.8: Turbulent kinetic energy κ

Boundary	Boundary condition
Inlet	fixedValue
Outlet	zeroGradient
Walls	kqRWallFunction
Cover inter vessel	slip
Cover cold	slip
Cover barrel	slip
Cover hot	slip